Physics – Uspekhi **61** (9) 825 – 845 (2018)

REVIEWS OF TOPICAL PROBLEMS PACS numbers: **71.35.–y**, 73.20.Mf, **78.67.–n**

Excitons and trions in two-dimensional semiconductors based on transition metal dichalcogenides

M V Durnev, M M Glazov

DOI: https://doi.org/10.3367/UFNe.2017.07.038172

Contents

Abstract. Theoretical and experimental results on excitonic effects in monomolecular layers of transition metal dichalcogenides are reviewed. These two-dimensional semiconductors exhibit a direct bandgap of about 2 eV at the Brillouin zone edges, and the binding energies of their neutral and charged excitons are in the range of hundreds and tens of millielectronvolts, respectively. This implies that electron–hole complexes determine the optical properties of transition metal dichalcogenide monolayers. Topics discussed in this review include the band structure details needed to understand the excitonic effects in these materials, the structure and fine structure of exciton and trion energy levels, the features of the spin and valley dynamics of Coulomb complexes, and how neutral and charged excitons manifest themselves in linear and nonlinear optical effects.

Keywords: transition metal dichalcogenides monolayers, Coulomb interaction, exchange interaction, exciton, trion, spin dynamics, valley dynamics, optical orientation, two-photon absorption, second harmonic generation, Zeeman effect

1. Introduction

In recent years, interest has strongly grown in two-dimensional semiconductor materials, the most prominent representative of which proved to be graphene — a monolayer of carbon atoms ordered into a hexagonal lattice [1–6]. Breakthrough studies of graphene led to interest in other two-dimensional systems as well, including the monolayers of hexagonal boron nitride, black phosphorus, and monolayers of transition metal dichalcogenides (TMDs) [7, 8]. Besides the unusual physical properties of two-dimensional crystals, the prospects of creating a new class of nanosystems — van der Waals heterostructures, in which the monatomic or monomolecular layers of different materials are superimposed on each other in a given sequence — are actively being discussed at present [9].

Among the wide family of two-dimensional semiconductors, a special place is occupied by the monomolecular layers of TMDs described by the formula MX_2, where M is a transition metal, and X is a chalcogen. The most studied representatives of this class of semiconductors are systems based on group VI elements of the Periodic Table, where $M =$ Mo or W, and the chalcogens are represented by S, Se, or Te. These materials were investigated in the bulk form in the 1960s and 1970s [10–12]; such crystals demonstrate semiconductor properties with an indirect band gap energy on the order of 1 eV. The situation changes qualitatively when going over from the bulk material to the monolayer. It turns out that many two-dimensional TMDs, including their most widespread representatives MoS_2, WS_2, $MoSe_2$, and WSe_2, become direct-band semiconductors with a bandgap energy of about 2 eV [13, 14]. This circumstance spurred the interest of researchers in MX_2 monolayers [15, 16].

Similarly to graphene, the atoms in the monolayers of TMDs are ordered into a hexagonal lattice (Figs 1a, b). The Brillouin zone of the MX_2 monolayers is hexagonal and, just as in graphene, the most interesting optical and transport effects at present take place near the points $\mathbf{K}_{\pm}$ at the corners of the Brillouin zone (Fig. 1c). In contrast to graphene, where the valence band and the conduction band merge at these

M V Durnev, M M Glazov Ioffe Institute, Russian Academy of Sciences, ul. Politekhnicheskaya 26, 194021 St. Petersburg, Russian Federation
E-mail: glazov@coherent.ioffe.ru

Received 4 July 2017, revised 14 July 2017
Uspekhi Fizicheskikh Nauk **188** (9) 913 – 934 (2018)
DOI: https://doi.org/10.3367/UFNr.2017.07.038172
Translated by S N Gorin; edited by A Radzig

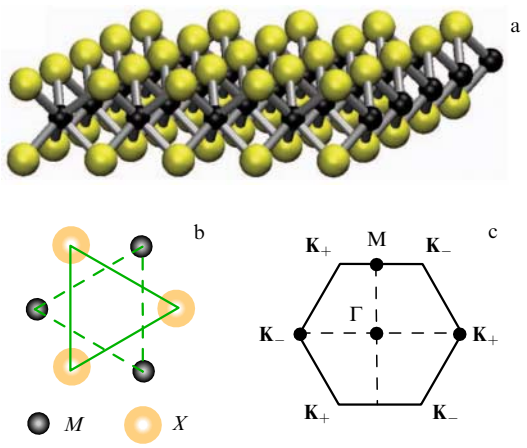

Figure 1. (Color online.) Schematic representation of the crystal structure of an MX_2 monolayer: (a) side view; (b) top view, and (c) Brillouin zone with the designation of high-symmetry points.

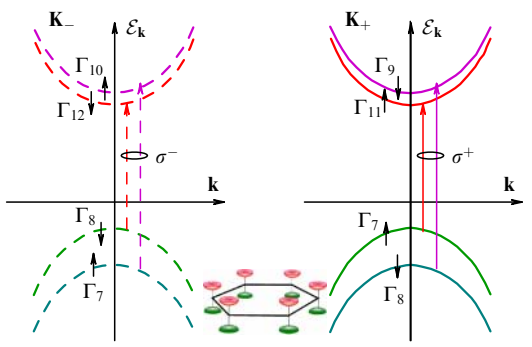

Figure 2. Schematic representation of the energy dispersion near the **K** points of the Brillouin zone and of the selection rules upon illumination by circularly polarized light for monolayers on the base of molybdenum (MoS_2 or $MoSe_2$). In the case of the WS_2 and WSe_2 monolayers, the spin subbands of the conduction band have a different order. In the inset, the Brillouin zone and the parabolic dispersion near the points $\mathbf{K}_\pm$ are schematically depicted.

points, a gap is opened in TMDs at the points $\mathbf{K}_\pm$ and a direct band gap is realized. Another important difference from graphene consists in the extremely strong spin-orbit interaction in MX_2 caused by the large atomic weight of transition metals. This circumstance leads to the removal of the spin degeneracy of the states in the valence band and in the conduction band in TMD monolayers at the points $\mathbf{K}_\pm$ of the Brillouin zone (Fig. 2); the spin splitting of the valence band is hundreds of millielectron-volts, and that of the conduction band from units to tens of millielectron-volts [17–20]. The signs of the spin splitting in the $\mathbf{K}_+$ and $\mathbf{K}_-$ valleys are opposite; therefore, the ground states of the electron and hole in each of the valleys possesses a specific spin, whose direction is locked to a specific valley in the energy spectrum. The competition of spin and valley degrees of freedom in the electronic properties of crystals can lead to unusual transport effects, for example, to the separation of the electronic states in different valleys under the action of an electric field — the valley Hall effect [21].

Monomolecular MX_2 layers also demonstrate unusual optical properties. First, by a normal incidence of radiation onto a monolayer, interband optical transitions in the $\mathbf{K}_+$ and $\mathbf{K}_-$ valleys are excited by photons with different helicities: σ^+ in the $\mathbf{K}_+$ valley, and σ^- in the $\mathbf{K}_-$ valley [22–26], which opens prospects for controling the valley degrees of freedom in these materials by polarized light. Moreover, the optical properties of the TMD monolayers are determined to a considerable degree by the neutral and charged excitons, i.e., the electron–hole complexes bound by Coulomb interaction. The binding energy of a neutral exciton in the MX_2 monolayer reaches hundreds of meV, and that of the charged exciton — the trion, which represents a three-particle complex consisting of two electrons and one hole or two holes and one electron — is tens of meV [27–32]. The Coulomb complexes are stable up to room temperature and possess a significant oscillator strength, and the analysis of the fine structure of their energy spectrum and of its manifestations in linear and nonlinear optical effects is one of the most urgent avenues of study today in the physics of two-dimensional materials.

The purpose of this review is to describe the state-of-the-art in the field of studies of electronic and exciton effects in TMD monolayers. In Section 2, basic models of the band structure of MX_2 monolayers are described; in Section 3, the structure of the exciton and trion is discussed, as is the fine structure of exciton energy levels. Sections 4 and 5 are devoted to manifestations of exciton properties in spin, valley, magneto-optical, and nonlinear optical effects.

2. Electronic properties

Knowledge of the band structure of MX_2 monolayers is a key to understanding the variety of exciton effects that appear in two-dimensional semiconductors. In this section, we give the minimum necessary information about the symmetry of electronic states in the $\mathbf{K}_+$ and $\mathbf{K}_-$ valleys of the Brillouin zone, which is the most important in the phenomena considered, give a brief review of atomistic methods, and describe the effective Hamiltonian method (**kp**-method), which makes it possible (with low computation costs, but with the retention of acceptable accuracy) to describe the details of the band structure and to take into account the interaction of charge carriers with each other and with external fields. A detailed analysis of the band structure of TMD monolayers can be found in review [17] and in a number of original studies, references to which will be given when necessary.

2.1 Band structure. Symmetry analysis

The symmetry of one monomolecular layer of a semiconductor belonging to the family of dichalcogenides of transition metals (see Fig. 1) is described by the point group D_{3h} without the center of inversion. This group contains the following elements of symmetry: the horizontal reflection plane σ_h passing through metal atoms; the axis of rotation of the third order C_3, perpendicular to the monolayer and passing through the center of a hexagon; mirror rotation axis S_3; three rotation axes of the second order C_2, which lie in the plane σ_h, and three reflection planes σ_v, which contain the C_2 axes. The unit cell of a two-dimensional crystal consists of one atom of metal and two atoms of chalcogen, located in the planes lying above and below the metal atom (Fig. 1a).

The Brillouin zone of the MX_2 monolayer has the shape of a regular hexagon; its high-symmetry points Γ, M, and $\mathbf{K}_\pm$ are shown in Fig. 1c. The direct energy gap is realized in the nonequivalent valleys $\mathbf{K}_\pm$ at the edges of the Brillouin zone, which are connected via the operation of time inversion. The symmetry of one valley is lower than the symmetry of the

monolayer on the whole; the symmetry group of the wave vector at the points $\mathbf{K}_\pm$ is C_{3h}. First-principles calculations show that the conduction band at the $\mathbf{K}$ points is mainly formed by the orbitals of the metal atoms which have the symmetry d_{z^2}, whereas the valence band is mainly contributed by $d_{(x\pm iy)^2}$ orbitals [20, 33], where x and y are the Cartesian coordinates in the plane of the layer, the z-axis coincides with the normal to the layer, and the designations of the atomic orbitals that are standard in atomic physics are used: s (angular momentum 0), p (angular momentum 1), d (angular momentum 2), etc.

The symmetry of the electronic states in the C_{3h} group of the wave vector is defined by both the transformation of the corresponding atomic orbitals and by the phase factor $\exp(i\mathbf{K}_\pm\mathbf{R}_j)$, where $\mathbf{R}_j$ describes the positions of atoms in the lattice. As a result, the Bloch functions of the valence band at the $\mathbf{K}_\pm$ points, whose periodic parts are composed by $d_{(x+iy)^2}$ and $d_{(x-iy)^2}$ orbitals, are invariants, which are transformed according to the representation of the C_{3h} group denoted as A' [18] or Γ_1 [34]. The states of the conduction band are transformed in the $\mathbf{K}_+$ and $\mathbf{K}_-$ valleys according to the representation $E_1'(\Gamma_2)$ as the function $x+iy$, and according to the representation $E_2'(\Gamma_3)$ as the function $x-iy$, respectively. It follows from the given symmetry analysis that in the case of normal incidence of radiation, the optical transitions from the valence band to the conduction band occur under the action of circularly polarized light; moreover, the transitions in the $\mathbf{K}_+$ and $\mathbf{K}_-$ valleys are active in the circular polarizations σ^+ and σ^-, respectively [22–26].

For the analysis of a wide range of physical phenomena in the MX_2 monolayers, extended models of the band structure are constructed, which take into account, apart from the lowest-energy conduction band and the highest-energy valence band, a number of 'remote' bands (see the diagram in Fig. 3). The representations, according to which the electronic states in the higher-energy conduction bands (c + 1, c + 2) and in the lower-energy valence bands (v − 1, v − 2, v − 3) are transformed, are given in Table 1. Notice that the states in the c, v, c + 2, and v − 3 bands are even with respect to the transformation of reflection from the plane σ_h, whereas the states in the c + 1, v − 1, and v − 2 bands are odd with respect to this operation. The corresponding representations in Table 1 differ in the number of prime symbols in the superscript (one for the even, and two for the odd states).

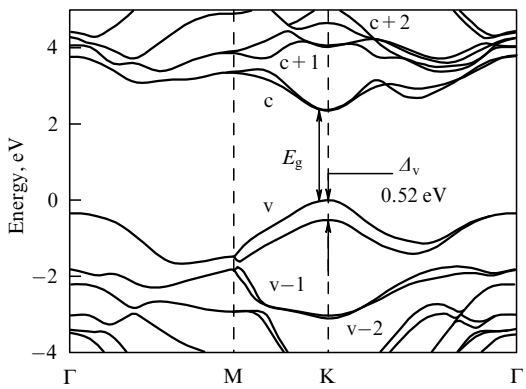

Figure 3. Calculating the band structure of the WSe_2 monolayer by the DFT method with a subsequent processing of the results within the framework of the GW approximation. The arrows designate the energy gap E_g between the c and v bands, and the spin-orbit splitting Δ_v of the valence band. (Adapted from Ref. [40].)

Table 1. Designations of electronic bands in TMD monolayers and the irreducible representations (without taking into account spin) of the group C_{3h} according to which the corresponding orbital states in the $\mathbf{K}_+$ and $\mathbf{K}_-$ valleys are transformed.

Representation		
$\mathbf{K}_+$	$\mathbf{K}_-$	Band
E_2'	E_1'	c + 2
A''	A''	c + 1
E_1'	E_2'	c
A'	A'	v
E_2''	E_1''	v − 1
E_1''	E_2''	v − 2
E_2'	E_1'	v − 3

When taking into account the electron spin, the states of the valence band are transformed according to the spinor representations Γ_7 (spin up, $s_z = +1/2$, where s_z is the projection of the spin onto the normal to the monolayer) and Γ_8 (spin down, $s_z = -1/2$) in each valley (see Fig. 2). The states of the conduction band in the $\mathbf{K}_+$ valley are transformed according to the representations Γ_{11} (spin up) and Γ_9 (spin down), and the states in the $\mathbf{K}_-$ valley according to Γ_{10} (spin up) and Γ_{12} (spin down). Since the electronic states with different projections of the spin onto the z-axis are transformed according to the different representations, the corresponding spin sublevels at the $\mathbf{K}_\pm$ points are split even in the absence of an external magnetic field. Because of the symmetry with respect to the time inversion, these splittings have opposite signs at the points $\mathbf{K}_+$ and $\mathbf{K}_-$ (see Fig. 2). The magnitudes of the spin splittings amount to ~ 100 meV for the valence band and increase with increasing atomic number of the constituent elements [35]. The spin subbands of the conduction band are split by $\sim 1-10$ meV; the order of magnitude of the splitting differs for the monolayers formed on the basis of molybdenum (MoS_2, $MoSe_2$) and on the basis of tungsten (WS_2, WSe_2) [19]. It should be emphasized that the optical transitions in the electric dipole approximation upon the propagation of light along the normal to a monolayer occur with the conservation of the spin and are determined only by the orbital component of Bloch functions; therefore, the selection rules do not change when taking into account spin: the transitions in the $\mathbf{K}_\pm$ valleys are active in $\sigma^\pm$ polarizations. A detailed analysis of optical transitions in different polarizations is given in Section 3.3.

2.2 Review of atomistic methods

The electronic structure of crystalline semiconductors is usually calculated using 'first-principles' (*ab initio*) methods (for example, by the density functional theory (DFT) method), which allow, using a minimum number of input parameters, obtaining the dispersion of the energy bands and the orbital composition of electronic states in the entire Brillouin zone. The DFT method is widely used for calculating the band structure of both the bulk crystals of dichalcogenides of transition metals and monolayers based on them; however, its computation difficulties and the complexity of taking into account external perturbations (such as magnetic field) limit its applicability for calculating physical effects.

At the same time, there is another class of methods, called empirical. Within the framework of the approaches of this class, the electronic states are described by the effective

multiband Hamiltonian, whose parameters are determined empirically, i.e., via a comparison of the observed values, obtained as a result of the diagonalization of a Hamiltonian, with the results of *ab initio* calculations and experimental data. The calculated dispersions of the bands and the orbital composition of wave functions can be used as the compared values, along with the experimental values of the effective masses and of the g-factors of charge carriers at the high-symmetry points of the Brillouin zone. The most common empirical methods are the empirical tight binding (TB) model and the **kp**-method of the perturbation theory.

Calculations of the energy dispersion of the bands by the DFT method with a subsequent treatment of the results obtained within the framework of the GW approximation to more correctly take into account the electron–electron interaction were performed in Refs [33, 36–40] (see also review [41]). The result of this calculation for the WSe_2 monolayer is illustrated in Fig. 3. The calculation was performed taking into account the spin-orbit interaction. The order of the bands corresponds to the designations in Table 1 (direct energy gap $E_g \approx 2.5$ eV is opened at the points **K** of the Brillouin zone between the bands c and v).

Let us now go over to a review of the empirical tight binding methods that are used widely in describing the electronic properties of MX_2 monolayers. The minimum tight binding model, which takes into account three d-type orbitals (d_{z^2}, $d_{(x+iy)^2}$, and $d_{(x-iy)^2}$) of the metal atoms, was developed in Ref. [20]. This three-band model makes it possible to obtain the dispersion of the c and v bands near the **K** points and the orbital composition of the corresponding wave functions that are close to the results of calculations by the DFT method.

In order to describe the electronic states in the entire Brillouin zone in the c and v bands, and also in the other, more distant conduction and valence bands, 11-band tight binding models are invoked, which include five d-orbitals of the metal atom and six p-orbitals of the chalcogen atoms [39, 42–44]. The effective Hamiltonian for these models is written out in the basis

$$\phi_j = \left\{ d_{z^2}, d_{(x+iy)^2}, d_{(x-iy)^2}, p_x^S, p_y^S, p_z^A, d_{xz}, d_{yz}, p_x^A, p_y^A, p_z^S \right\}, \quad (1)$$

where d_α denotes the d-symmetry orbital on the metal atom, while $p_\beta^S = (p_{\beta,t} + p_{\beta,b})/\sqrt{2}$ and $p_\beta^A = (p_{\beta,t} - p_{\beta,b})/\sqrt{2}$ are the symmetric and antisymmetric combinations of the p-orbitals of the upper (top) (t) and lower (bottom) (b) atoms of the chalcogen in the unit cell of the crystal.

The freely suspended monolayer is symmetric relative to the specular reflection $z \to -z$; therefore, the effective Hamiltonian $\mathcal{H}(\mathbf{q})$ of the multiband model for an electron with wave vector $\mathbf{q}$ in the basis (1) is separated into two independent blocks and takes on the form

$$\mathcal{H}(\mathbf{q}) = \begin{pmatrix} \mathcal{H}_E & 0 \\ 0 & \mathcal{H}_O \end{pmatrix}. \quad (2)$$

Here, $\mathcal{H}_E$ is a block of size 6×6, which acts on the orbitals that are even with respect to the operation $z \to -z$ [first six orbitals of the basis (1)], and $\mathcal{H}_O$ is a block of the size 5×5, which acts on the odd orbitals. The concrete form of matrices $\mathcal{H}_E$ and $\mathcal{H}_O$ depends on the details of the model [39, 42–44]. As was mentioned earlier, the Bloch functions of the bottom of conduction band (c) and of the top of valence band (v) are

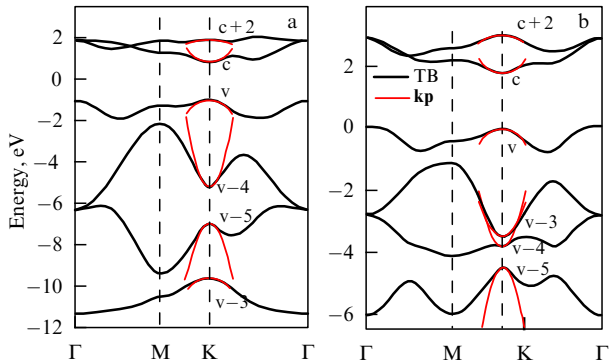

Figure 4. (Color online.) Electronic spectrum of MoS_2 calculated within the framework of the tight binding model presented in Refs [44] (a) and [39] (b). Only bands that correspond to states even relative to the reflection $z \to -z$ are given. Spin-orbit splitting was not taken into account in the calculations. Red (thin) lines depict parabolic dispersions at the **K** point with the effective masses calculated in the framework of the **kp**-method via formulas similar to Eqn (8). TB marks the tight binding method. (Figures were taken from Ref. [45].)

even with respect to the reflection operation $z \to -z$ and, therefore, these bands (as well as bands c + 2 and v − 3) are described by the block $\mathcal{H}_E$. Bands c + 1, v − 1, and v − 2 (see Table 1) enter into the composition of the block $\mathcal{H}_O$. It is important to note that the magnetic field directed along the normal to the monolayer does not break the parity of wave functions; therefore, it is possible to limit oneself to only the effective Hamiltonian $\mathcal{H}_E$ when calculating the Zeeman effect in bands c and v (see Section 4.1). The dispersions of even bands obtained within the framework of the tight binding model presented in Refs [44] and [39] are given in Fig. 4. Within this approach, the effects connected with the presence of a substrate or of an electric field applied along the normal to the MX_2 monolayer can be taken into account using the perturbation theory by mixing the $\mathcal{H}_E$ and $\mathcal{H}_O$ blocks.

2.3 Effective Hamiltonian method

The electronic states in the **K** valleys can also be described within the framework of the effective **kp** Hamiltonian. The simplest two-band **kp** model contains the states of bands v and c, which, without taking into account spin at points $\mathbf{K}_\pm$, transform as a scalar and as the $x \pm iy$ functions, respectively. The effective **kp** Hamiltonian $\mathcal{H}_{2,\pm}$, which describes states near points $\mathbf{K}_\pm$, can be constructed by the method of invariants, and in the linear approximation in wave vector $\mathbf{k}$ counted from the corresponding point $\mathbf{K}_\pm$ is written out as

$$\mathcal{H}_{2,+} = \begin{pmatrix} E_g & \gamma_3 k_- \\ \gamma_3 k_+ & 0 \end{pmatrix}, \quad \mathcal{H}_{2,-} = \begin{pmatrix} E_g & -\gamma_3 k_+ \\ -\gamma_3 k_- & 0 \end{pmatrix}. \quad (3)$$

Here, the energy is counted off from the top of the valence band, E_g is the energy gap, $k_\pm = k_x \pm ik_y$, $\mathbf{k} = (k_x, k_y)$ is the two-dimensional wave vector of the electron counted off from points $\mathbf{K}_\pm$, and γ_3 is the parameter proportional to the interband matrix element of the momentum operator. Notice that hereinafter parameter γ_3 is assumed to be real; it can be reached by the selection of the phases of the Bloch functions. Taking into account the electron spin, the effective Hamiltonian similar to that in formula (3) describes two independent pairs of states: pairs (Γ_7, Γ_{11}) and (Γ_8, Γ_9) in the $\mathbf{K}_+$ valley, and pairs (Γ_7, Γ_{10}) and (Γ_8, Γ_{12}) in the $\mathbf{K}_-$ valley, while the magnitude of E_g in this approach depends on the sign of the

spin component s_z and is equal to the energy difference between the corresponding levels at $\mathbf{k} = 0$. The diagonalization of Hamiltonian (3) yields symmetric dispersions of the conduction band and of the valence band with the effective masses $m_c = -m_v = m^*$, where

$$\frac{1}{m^*} = \frac{2\gamma_3^2}{\hbar^2 E_g} . \tag{4}$$

Calculations using the DFT method give values $m^* \approx 0.5m_0$ and $E_g \approx 2.5$ eV for most MX_2 monolayers investigated to date; these data make it possible to obtain a crude estimate for the interband parameter $\gamma_3 \approx 4$ eV Å. The magnitude of γ_3 in units of velocity corresponds to $\gamma_3/\hbar \approx c/500$, where c is the speed of light, and in energy units to $2m_0\gamma_3^2/\hbar^2 \approx 5$ eV. The values of the interband matrix element of the velocity operator of this order of magnitude are characteristic of other semiconductors as well [2, 46].

Although the two-band model (3) is sufficient for calculating the rate of optical transitions and the fine structure of the radiative exciton-doublet, it does not take into account several important features of the systems under consideration, including the asymmetry of the dispersion of the electron and hole in the **K** valleys, and the absence of the center of spatial inversion in the symmetry group C_{3h}. As will be shown further in Section 4.1, the two-band model also leads to equal-in-magnitude g-factors of the conduction band and valence band and, correspondingly, to the absence of splittings of the spin levels of excitons in a magnetic field, which contradicts experimental data. These features can be taken into account by introducing into the effective Hamiltonian additional bands of the same parity, in particular, the adjacent bands c + 2 and v − 3 (see Table 1 and Fig. 4). The effective Hamiltonian of the obtained four-band model can be found with the aid of the method of invariants and has the following form in the $\mathbf{K}_+$ valley [18]:

$$\mathcal{H}_{4,+}(\mathbf{k}) = \begin{pmatrix} E_{v-3} & \gamma_2 k_+ & \gamma_5 k_- & 0 \\ \gamma_2 k_- & E_v & \gamma_3 k_+ & \gamma_4 k_- \\ \gamma_5 k_+ & \gamma_3 k_- & E_c & \gamma_6 k_+ \\ 0 & \gamma_4 k_+ & \gamma_6 k_- & E_{c+2} \end{pmatrix} , \tag{5}$$

where γ_j ($j = 2-6$) are real (owing to the choice of the phases of appropriate Bloch functions) parameters, and E_n is the energy of the band with the number n at $\mathbf{k} = 0$. The corresponding Hamiltonian in the $\mathbf{K}_-$ valley is obtained via the operation $k_\pm \to -k_\mp$. Hamiltonian (5) takes into account the trigonal symmetry of the crystal lattice and the absence of the center of spatial inversion. In order to illustrate this property, let us calculate with the aid of a **kp**-method the effective matrix element, which mixes the c and v bands and is proportional to the second power of the wave vector. In the second-order perturbation theory, we obtain

$$V_{v,c}^{(\mathbf{K}_\pm)} = \mp \frac{1}{2} A\gamma_3 k_\mp^2 \propto k_\mp^2 , \tag{6}$$

where a parameter A was introduced according to the relationship

$$A = \frac{1}{\gamma_3}\left(\frac{\gamma_4\gamma_6}{E_{c+2} - E_c} + \frac{\gamma_4\gamma_6}{E_{c+2} - E_v} - \frac{\gamma_5\gamma_2}{E_v - E_{v-3}} - \frac{\gamma_5\gamma_2}{E_c - E_{v-3}}\right) . \tag{7}$$

Thus, the mixing of the conduction band and of the valence band is accomplished, apart from the linear-in-the-wave-vector terms $k_\pm$, also by quadratic contributions $\propto k_\mp^2$. This fact reflects the absence of the center of inversion in the material, as well as the trigonal symmetry of the **K** valleys, since the symmetry group C_{3h} contains the three-fold axis, and the function $(k_x - \mathrm{i}k_y)^2 \propto \exp(-\mathrm{i}2\varphi)$, where φ is the angle between **k** and the x-axis, is transformed in this group just like the function $k_x + \mathrm{i}k_y \propto \exp(\mathrm{i}\varphi)$.

The effective masses in the c and v bands are expressed through the parameters of Hamiltonian (5) as follows [47]:

$$\begin{aligned} \frac{1}{m_c} &= \frac{2}{\hbar^2}\left(\frac{\gamma_5^2}{E_c - E_{v-3}} + \frac{\gamma_3^2}{E_c - E_v} + \frac{\gamma_6^2}{E_c - E_{c+2}}\right) , \\ \frac{1}{m_v} &= \frac{2}{\hbar^2}\left(\frac{\gamma_2^2}{E_v - E_{v-3}} + \frac{\gamma_3^2}{E_v - E_c} + \frac{\gamma_4^2}{E_v - E_{c+2}}\right) , \end{aligned} \tag{8}$$

so that $m_c \neq m_v$. The Hamiltonian constructed above makes it possible to calculate the g-factor of the exciton (see Section 4.1) and to describe the effects connected with the noncentrosymmetry of the monolayer, in particular, the generation of the second optical harmonic (see Section 5.2). For a number of applications, the symmetry of the crystal lattice can also be reproduced by retaining, in the expansion of the two-band **kp** Hamiltonian in powers of the wave vector, the nondiagonal contributions quadratic in **k** [see Eqn (6)] and the diagonal contributions cubic in **k**, connected with taking into account the remote bands according to the perturbation theory [17]. The approach based on Hamiltonian (5) possesses the advantage allowing us to take into account only interband matrix elements that are linear in **k**.

For the successful application of **kp**-models, it is necessary to derive the parametrization of the effective Hamiltonian. In concrete calculations, it is convenient to apply the approach realized in paper [45]. Within the framework of this method, the phenomenological parameters of Hamiltonian (5) can be unambiguously determined using the expansion of the effective Hamiltonian $\mathcal{H}_E(\mathbf{q})$ of the tight binding model near the **K** points ($\mathbf{k} = \mathbf{q} - \mathbf{K}_\pm$):

$$\mathcal{H}_{4,\pm}(\mathbf{k}) \approx \mathcal{H}_E(\mathbf{K}_\pm) + \sum_{\alpha=x,y} \frac{\partial \mathcal{H}_E}{\partial q_\alpha}(\mathbf{K}_\pm) k_\alpha . \tag{9}$$

Here, the first term of the expansion determines the diagonal energies E_n, and the second term the contributions linear in the wave vector, which are proportional to the coefficients γ_j. The parameters of the tight binding model can be determined by using it to fit the results of calculations of the energy dispersion and orbital composition of the wave functions in the DFT method over the entire Brillouin zone. Further, this approach is used in analyzing the Zeeman effect in MX_2 monolayers; the main parameters of the band structure of the MX_2 monolayers obtained are given in Table 2.

3. Coulomb complexes: excitons and trions

Exciton states in crystals have been studied since the 1930s [48–51]. Special interest in exciton effects appeared in the 1950s, after Gross and Karryev [52] revealed a hydrogen-like series of exciton states in cuprous oxide. As a result of numerous experimental and theoretical studies, it was established that many optical properties of semiconductor crystals were caused by the presence of hydrogen-like complexes, which consist of an electron and a hole bound by Coulomb attraction. In this section, we discuss the specific

Table 2. Band parameters of TMD monolayers found in Ref. [45] on the basis of calculations using the density-functional-theory method (DFT + GW) and the tight binding method. Parameters from Ref. [17] are given in parentheses for MoS_2 (averaged values for different DFT + GW realizations and, in the case of effective masses, averaged over two spin subbands).

	MoS_2	$MoSe_2$	WS_2	WSe_2
E_g, eV	2.49 (2.84)	2.32	3.01	2.43
Δ_v, meV*	148	185	427	464
Δ_c, meV*	3	21	−32	−37
m_v/m_0	−0.56 (−0.58)	−0.57	−0.49	−0.58
m_c/m_0	0.37 (0.45)	0.52	0.40	0.46
g_v	5.59	5.83	5.96	4.08
g_c	1.77	3.21	2.11	0.24
$g_{X^0} = g_c - g_v$	−3.82	−2.62	−3.85	−3.84

* Adapted from Ref. [17].

features of exciton states in TMD monolayers caused by both the peculiarities of Coulomb interaction in thin films and by the fine structure of electronic states (due to the presence of two valleys and a strong spin-orbit interaction).

3.1 Coulomb interaction in thin films

In contrast to the widespread structures with quantum wells consisting of III–V and II–VI semiconductors, the structures based on TMD monolayers are characterized by a significant contrast in dielectric properties. Most vividly, this can be manifested for freely suspended monolayers surrounded by air or vacuum, since the dielectric constant of bulk MX_2 crystals, according to different estimations, is on the order of 10 and in this case considerably exceeds the dielectric constant of the environment.[1]

The potential of the electrostatic field created by a point charge in a thin film placed between two bulk dielectrics was calculated in Refs [53, 54], in which a film of a finite thickness d prepared from a material with the dielectric constant ϵ and surrounded by media with the dielectric constants ϵ_1 and ϵ_2 was studied, and the approach was invoked based on the application of the macroscopic equations of electrodynamics. This approach cannot be directly applied to the monomolecular layers of TMDs, since it implies averaging over the volume containing many unit cells of the crystal [55, 56]. However, a similar expression for the effective potential can be obtained by analyzing the two-dimensional limit, in which the thickness of the film is disregarded, and the dielectric response of the film is characterized by the two-dimensional susceptibility α_{2D} according to the expression

$$\mathbf{P} = \delta(z)\alpha_{2D}\mathbf{E}_{\parallel}\,, \tag{10}$$

where $\mathbf{P}$ is the dielectric polarization, i.e., the dipole moment of a unit volume, $\mathbf{E}_{\parallel}$ is the two-dimensional vector comprising the field components in the plane of the layer, and the Dirac δ function reflects the circumstance that the entire dipole moment is induced in the two-dimensional film, which occupies the plane $z = 0$. Following paper [57], let us calculate the electrostatic potential induced by the point charge e located in a film at the origin of the coordinates. For this purpose, let us introduce the charge density $n_{\text{ext}}(\mathbf{r}) = e\delta(\mathbf{r})$. The electrostatic potential $\varphi(\mathbf{r})$ created by the charge in the entire space satisfies Poisson's equation

$$\Delta\varphi(\mathbf{r}) = -4\pi n(\mathbf{r})\,, \tag{11}$$

where $n = n_{\text{ext}} + n_{\text{ind}}$ is the sum of the densities of the point charge and the charge induced in the film, n_{ind}. The density of the induced charge can be expressed through the polarization vector $\mathbf{P}$ of the film as $n_{\text{ind}} = -\operatorname{div}\mathbf{P}$. In turn, the polarization vector is connected with the component of the electric field in the plane of the film, $\mathbf{E}_{\parallel} = -\nabla_{\boldsymbol{\rho}}\varphi(\boldsymbol{\rho}, z = 0)$, in accordance with expression (10). Taking into account the charge induced in the film, namely

$$n_{\text{ind}}(\mathbf{r}) = \delta(z)\alpha_{2D}\Delta_{\boldsymbol{\rho}}\varphi(\boldsymbol{\rho}, z = 0)\,, \tag{12}$$

the equation for the potential $\varphi(\mathbf{r})$ takes on the form

$$\Delta\varphi(\mathbf{r}) = -4\pi e\delta(\mathbf{r}) - 4\pi\alpha_{2D}\delta(z)\Delta_{\boldsymbol{\rho}}\varphi(\boldsymbol{\rho}, z = 0)\,. \tag{13}$$

This equation is solved with the aid of the Fourier transform

$$\varphi(\mathbf{q}, k_z) = \int \mathrm{d}z \int \mathrm{d}\boldsymbol{\rho}\, \varphi(\boldsymbol{\rho}, z) \exp\left(-\mathrm{i}k_z z - \mathrm{i}\mathbf{q}\boldsymbol{\rho}\right), \tag{14}$$

where $\mathbf{q}$ and k_z are the components of the wave vector in the plane of the film and along the z-axis, respectively. From the solution to equation (13), we obtain the Fourier component $\varphi_{2D}(\mathbf{q}) = (2\pi)^{-1}\int \mathrm{d}k_z\, \varphi(\mathbf{q}, k_z)$ of the two-dimensional potential in the plane of the film:

$$\varphi_{2D}(\mathbf{q}) = \frac{2\pi e}{|\mathbf{q}|\left(1 + 2\pi\alpha_{2D}|\mathbf{q}|\right)}\,. \tag{15}$$

Notice that the obtained potential coincides in form with the potential of the point charge in a two-dimensional medium with the effective dielectric constant $\tilde{\epsilon}(\mathbf{q}) = 1 + 2\pi\alpha_{2D}|\mathbf{q}|$, which depends on the wave vector.

The reverse transformation into the $\mathbf{r}$ space gives

$$\varphi_{2D}(\boldsymbol{\rho}) = \varphi(\boldsymbol{\rho}, z = 0) = \frac{\pi e}{2r_0}\left[\mathrm{H}_0\left(\frac{\rho}{r_0}\right) - \mathrm{Y}_0\left(\frac{\rho}{r_0}\right)\right], \tag{16}$$

where H_0 and Y_0 are the Struve and Neumann functions, respectively, and

$$r_0 = 2\pi\alpha_{2D}\,. \tag{17}$$

Formula (16) describes the potential of the field of the point charge screened by the two-dimensional film, with the parameter r_0 having meaning of the screening length (Fig. 5). On the spatial scales that exceed the screening length, $\rho/r_0 \gg 1$, we have

$$\varphi_{2D}(\boldsymbol{\rho}) \approx \frac{e}{\rho}\,, \tag{18}$$

which coincides with the field of the unscreened charge. In the opposite case, for $\rho/r_0 \ll 1$, the potential has a logarithmic asymptotic form:

$$\varphi_{2D}(\boldsymbol{\rho}) \approx -\frac{e}{r_0}\left(\ln\frac{\rho}{2r_0} + C\right), \tag{19}$$

where C is the Euler constant, which corresponds to the effective screening of the external field by the film.

[1] Notice that in the bulk TMD crystals the tensor of the dielectric constant has two independent components, $\epsilon_{\parallel}$ and $\epsilon_{\perp}$, which describe the screening of the fields parallel and perpendicular to the c-axis. The estimates obtained in Ref. [27] for bulk MoS_2 give $\epsilon_{\parallel} = 6.3$ and $\epsilon_{\perp} = 13$.

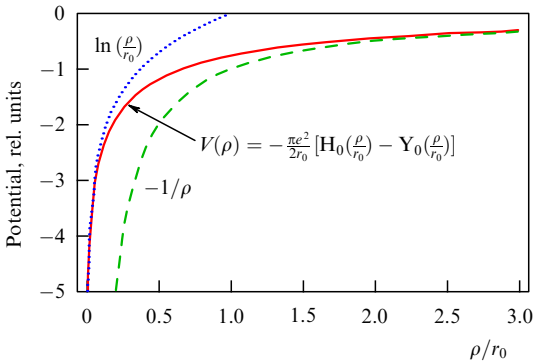

Figure 5. (Color online.) Energy of interaction of two point charges of opposite signs, which are located on a thin film at a distance ρ from each other: $V(\rho) = -e\varphi_{2\mathrm{D}}(\rho)$. The dashed and dotted lines show the asymptotic forms of the potential at large and small distances.

In the more general case, when the film is placed between two dielectrics with permittivities ϵ_1 and ϵ_2, potential (16) is modified by the substitution of $r_0' = 2r_0/(\epsilon_1 + \epsilon_2)$ for r_0 in the arguments of the Struve and Neumann functions. For a film of a finite (macroscopic) thickness d with a dielectric constant ϵ, the parameter $\alpha_{2\mathrm{D}}$ is given by the expression

$$\alpha_{2\mathrm{D}} = d\,\frac{\epsilon - 1}{4\pi}\,, \tag{20}$$

which allows, in the limiting case of $\epsilon \gg 1$, going over from formula (16) to formula (2) from paper [54], and to formula (8) from paper [53].

Calculations of $\alpha_{2\mathrm{D}}$ for the monolayers of different TMDs, including MoS_2, $MoSe_2$, WS_2, and WSe_2, were carried out in Ref. [30]. To this end, the first-principles methods were applied to calculate the component $\epsilon_\perp$ of the tensor of the dielectric constants in the direction perpendicular to the c-axis of the bulk structure comprising periodically alternating monolayers and empty spaces of width L. Using the obtained values of $\epsilon_\perp(L)$, the parameter $\alpha_{2\mathrm{D}}$ can be calculated as a following limit:

$$\alpha_{2\mathrm{D}} = \lim_{L\to+\infty} L\,\frac{\epsilon_\perp(L) - 1}{4\pi}\,. \tag{21}$$

The calculated values vary in the range of $\alpha_{2\mathrm{D}} \approx 5-8$ Å for different materials; the corresponding values of r_0 lie in the range of 30–50 Å. A crude estimate for $\alpha_{2\mathrm{D}}$ can be made via formula (20) if we use the value of $\epsilon_\perp$ for the bulk crystal as the value of ϵ, and as the value of d the distance between the atomic layers in the bulk crystal [30].

3.2 Binding energy of the exciton. 'Rydberg' series

The optical properties of bulk semiconductors and semiconducting nanostructures are to a considerable degree determined by the presence of exciton excitations, which are the bound states of an electron and hole interacting according to the Coulomb law [58, 59]. The binding energy of an exciton in widespread bulk semiconductors (GaAs, CdTe, ZnO, Cu_2O) is on the order of units and tens of millielectron-volts [58]. In low-dimensional structures, the binding energy increases owing to the localization of an electron and hole in one or several spatial directions and, correspondingly, to an increase in the Coulomb attraction of charge carriers [60, 61]. In the case of excitons in freely suspended crystalline monolayers, their binding energy can be even larger due to the absence of the electric field screening in a vacuum. Thus, the binding energy of excitons in two-dimensional semiconductors can reach already hundreds of millielectron-volts, which is sufficient for investigating exciton effects at room temperature.

In this section, we will examine the states of a two-dimensional exciton in monomolecular layers of TMDs. We are interested in the excitons formed by an electron and hole with the wave vectors near the $\mathbf{K}_\pm$ points of the Brillouin zone. In the smooth envelopes method, the wave function of an exciton that is at rest as a whole can be written out in the first approximation as follows [61–63]:

$$\Psi_{\mathrm{X}}^{\pm}(\boldsymbol{\rho}_{\mathrm{e}}, \boldsymbol{\rho}_{\mathrm{h}}) = \psi(\boldsymbol{\rho}_{\mathrm{e}} - \boldsymbol{\rho}_{\mathrm{h}})\, u_{\mathrm{c},\mathbf{K}_\pm}(\boldsymbol{\rho}_{\mathrm{e}})\, \tilde{u}_{\mathrm{v},\mathbf{K}_\mp}(\boldsymbol{\rho}_{\mathrm{h}})\,, \tag{22}$$

where $\boldsymbol{\rho}_{\mathrm{e}}$ and $\boldsymbol{\rho}_{\mathrm{h}}$ are the coordinates of the electron and the hole, $\psi(\boldsymbol{\rho})$ is the smooth function of the relative motion of the electron and the hole, $u_{\mathrm{c},\mathbf{K}_\pm}(\boldsymbol{\rho}_{\mathrm{e}})$ and $u_{\mathrm{v},\mathbf{K}_\pm}(\boldsymbol{\rho}_{\mathrm{h}})$ are the Bloch functions of the conduction band and of the valence band at the $\mathbf{K}_\pm$ points of the Brillouin zone, and the tilde designates that the function of the valence band is taken in the hole representation. Hereinafter, for brevity, we omit the dependence of the Bloch functions on the coordinate z along the normal to the monolayer. It should be noted that the two-particle Bloch function $u_{\mathrm{c},\mathbf{K}_+}(\boldsymbol{\rho}_{\mathrm{e}})\tilde{u}_{\mathrm{v},\mathbf{K}_-}(\boldsymbol{\rho}_{\mathrm{h}})$ in formula (22) corresponds to the excited state of the crystal, wherein the state of the conduction band in the $\mathbf{K}_+$ valley is occupied, and the state of the valence band in the same $\mathbf{K}_+$ valley is free. The hole in this case is associated with the state in the $\mathbf{K}_-$ valley that is connected with the initial state by the operation of time inversion [64]. The spin indices of the electron and of the hole are considered to be included in the subscripts c and v numbering the bands.

In the effective mass approximation, the equation for the $\psi(\boldsymbol{\rho})$ function is written out as follows:

$$-\frac{\hbar^2}{2\mu}\,\Delta_{\boldsymbol{\rho}}\psi(\boldsymbol{\rho}) + V(\rho)\psi(\boldsymbol{\rho}) = E\psi(\boldsymbol{\rho})\,, \tag{23}$$

where $\mu^{-1} = m_{\mathrm{c}}^{-1} + m_{\mathrm{v}}^{-1}$ is the reduced mass of the electron and hole, and $V(\rho) = -e\varphi_{2\mathrm{D}}(\rho)$ is the electrostatic interaction potential of the electron and hole (16), which takes into account the specific character of screening by the material of the film. Further, we will use the scale of length $a_0 = \hbar^2\epsilon/\mu e^2$ and the scale of energy $E_0 = \mu e^4/2\hbar^2\epsilon^2$, which correspond to the Bohr radius and binding energy of a three-dimensional exciton in a material with the averaged dielectric constant of the environment $\epsilon = (\epsilon_1 + \epsilon_2)/2$. In these units, equation (23) takes on the form

$$-\Delta_{\boldsymbol{\xi}}\psi(\boldsymbol{\xi}) - \pi\eta\left[\mathrm{H}_0(\eta\xi) - \mathrm{Y}_0(\eta\xi)\right]\psi(\boldsymbol{\xi}) = \epsilon\psi(\boldsymbol{\xi})\,, \tag{24}$$

where the dimensionless parameter $\eta = \epsilon a_0/r_0$ is the only parameter of the problem.

It follows from equation (24) that in the problem under consideration two limiting cases can be separated. In the limit of weak screening ($\eta \gg 1$), the potential of the interaction is $V(\rho) \approx -e^2/\epsilon\rho$, and the problem is reduced to the determination of the states of the two-dimensional exciton in the Coulomb potential. In this case, the characteristic size of the wave function for the ground state is a_0 and increases upon increasing the principal quantum number n, and the energy of the exciton is $E_n = -4E_0/(2n-1)^2$, $n \geqslant 1$. In the opposite

limit of the strong screening ($\eta \ll 1$), the spectrum of the exciton energy levels takes on the form [54]

$$E_n = 2\eta E_0 \left(\frac{1}{2} \ln \eta - \frac{3}{2} \ln 2 + C + \gamma_n \right), \tag{25}$$

where the numbers γ_n are the eigenvalues of the equation

$$-\Delta_\zeta \psi(\zeta) + \ln \zeta \, \psi(\zeta) = \gamma \psi(\zeta), \tag{26}$$

satisfying the conditions of the finiteness of the function ψ as $|\zeta| \to 0$, and $\psi \to 0$ as $|\zeta| \to \infty$. The characteristic size of the exciton wave function of the ground state in this case is equal to [54]

$$a = \frac{a_0}{\sqrt{2\eta}} = \sqrt{\frac{a_0 r_0}{2\epsilon}} = \sqrt{\frac{\hbar^2 r_0}{2\mu e^2}}; \tag{27}$$

it is determined only by the polarizability of the two-dimensional crystal [see formula (17)] and does not depend on the quantity ϵ, i.e., on the dielectric environment. From equation (26), it follows that $\gamma_n \sim 1$; in this case, $-\ln \eta \gg 1$ for $\eta \ll 1$; therefore, the energy E_n is much more than the distance between the adjacent energy levels. It follows from Eqn (25) that in the limit $\eta \to 0$ the energy E_n tends to zero.

The result of the numerical solution to equation (24) in a wide range of values of the parameter η is shown in Fig. 6. This figure plots the energy of the ls state of the exciton and the relative splitting between the 2s and the 2p levels $(E_{2s} - E_{2p})/E_{2s}$ as a function of η. It can be seen that in the limit of $\eta \gg 1$, where the potential $V(\rho)$ is Coulombic, the energy of the ls state of an exciton takes on the value $-4E_0$, and the states 2s and 2p are degenerate in energy. The 'accidental' degeneracy of the spectrum in terms of the value of the angular momentum, however, is lifted for finite η, when the potential of interaction differs from the Coulomb potential. The absolute value of the binding energy of the exciton states in this case is less than the two-dimensional Coulomb potential, since the electrostatic field between the electron and hole predominantly (for $\eta \lesssim 1$) is screened by the two-dimensional film.

A calculation of the binding energy of the ground state of the exciton by the effective mass method was carried out in paper [30] for different TMD monolayers. In that study, a trial wave function $\psi(\boldsymbol{\rho}) \sim \exp(-\rho/\tilde{a})$ with the variation parameter $\tilde{a}$ was used. The obtained values of the binding energy and of the exciton radius for an MoS_2 film freely suspended in a vacuum ($\epsilon = 1$) are $E_{1s} = 0.54$ eV and $a = 10.4$ Å, respectively. In the calculation, the values of $\mu = 0.25 m_0$ and $r_0 \approx 41$ Å were utilized, so that $a_0 = 2.1$ Å and of $\eta \approx 0.05$, which corresponds to the regime of strong screening (see Fig. 6). The calculations for other systems ($MoSe_2$, WS_2, and WSe_2) also predict values of the binding energy on the order of 0.5 eV.

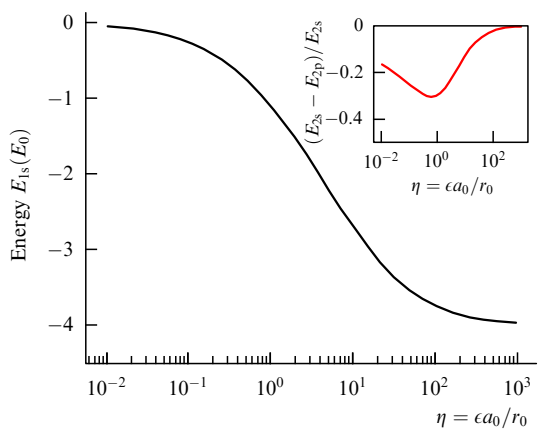

Figure 6. (Color online.) Energy of the ground state of an exciton and relative splitting between 2s and 2p states (in the inset) as functions of a dimensionless parameter η.

Experimental studies of a Rydberg series in monolayers of different materials have been performed in a number of papers, for example, in Refs [27–29]. In Ref. [27], the spectrum of the reflection coefficient of WS_2 monolayers on a substrate of SiO_2/Si was measured near exciton resonances. The series of energy levels of ns excitons, E_{ns}, for $n = 1-5$, obtained from the processing of experimental data, is given in Fig. 7. This series is described well by the numerical solutions of equation (23) with the potential (16) at $\mu = 0.16 m_0$ and $r_0 = 75$ Å. The corresponding binding energy of the 1s exciton is $E_{1s} = 0.32$ eV. It is worthwhile to note that the value of E_{1s} obtained in the study is less than that calculated in Ref. [30] for the WS_2 monolayer in a vacuum. This can be explained by the presence of a substrate with $\epsilon > 1$ in the experiment, which leads to an additional screening of the electric field [27]. For comparison, Fig. 7a also shows the dependence of E_n for the case of a Coulomb potential. It can be seen that for excited exciton states, whose size exceeds the screening length ($n = 3-5$), the behavior of the energy levels is described well by the model of a Coulomb potential, while the binding energy of the ground state is substantially less than that in the Coulomb potential model. For an approximate description of the energies of a nonhydrogen-like series, the authors of Ref. [27] introduced an effective dielectric constant ϵ_n of the sample, which depends on the energy of the state (see the insets to Figs 7a and 7c).

The influence of the dielectric properties of the environment on the parameters of two-dimensional excitons was experimentally investigated, for example, in Refs [65–67]. In particular, in Ref. [66], the diamagnetic shift of the exciton lower energy level was measured in a WSe_2 monolayer placed between media with different dielectric constants, and on the basis of these measurements the dependences of the binding energy and characteristic size of the wave function of exciton on the parameter ϵ were obtained. The results obtained — a decrease in the binding energy and an increase in the size of the exciton with the increase in ϵ — are in agreement with the predictions of the model presented here.

The above approach to the description of exciton states in monomolecular crystalline layers, based on the smooth envelopes method, gives a qualitative and a quantitative representation of the behavior of exciton energy levels, and the results of calculations agree rather well with the experimental values of the binding energy of excitons. On the other hand, the measured values of the exciton binding energy and of the exciton radius ($E_{1s} \sim 400$ meV, $a \sim 10$ Å) lie on the boundaries of the applicability of the smooth envelopes method, which requires that the wave function of the exciton cover a large number of unit cells in the crystal. The calculations of the exciton spectrum taking into account the electronic states in the entire Brillouin zone were performed with the employment of atomistic methods, such as the DFT method [33, 36, 37] and the tight binding method [68], in combination with the Bethe–Salpeter equation, which takes into account the electrostatic interaction between the electron and hole. In the above-listed works, values were obtained for

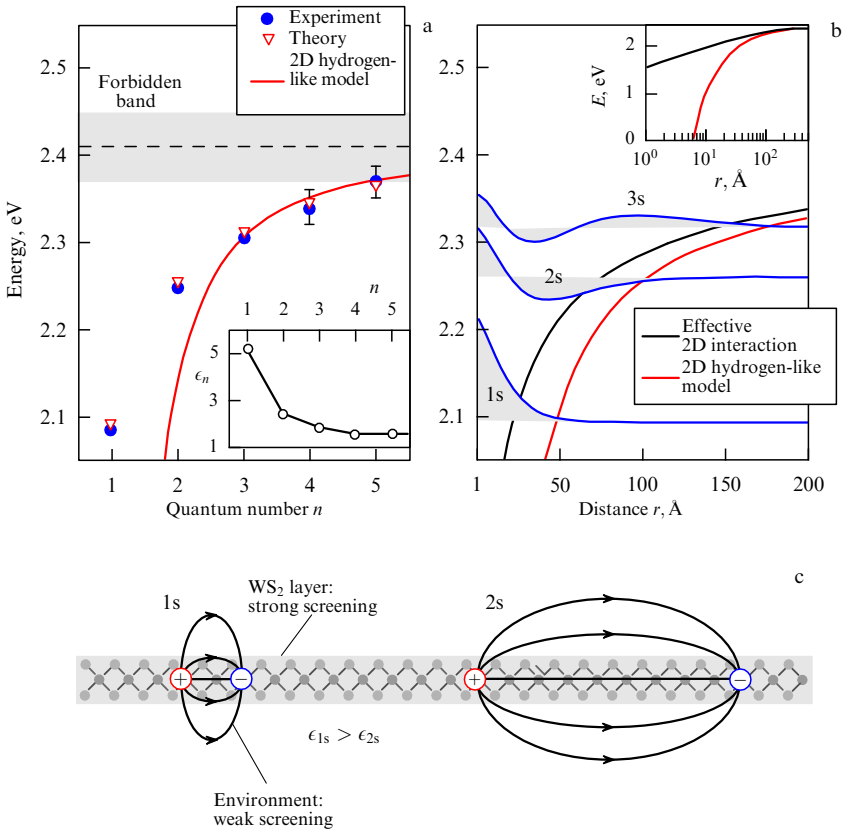

Figure 7. (Color online.) Energy of exciton states in the WS_2 monolayer. (a) Experimental values of the energy corresponding to the positions of the features in the reflection spectrum in the region of exciton resonances, and the corresponding calculation based on the solution to equation (23). The solid line shows the spectrum of exciton states in the Coulomb-potential model; in the inset, the values of the effective dielectric constant ϵ_n are given. (b) Potential (16) screened by the film and the Coulomb potential $\sim 1/\rho$; in the inset, the same dependences are depicted on a semilogarithmic scale. In addition, graphs of the wave functions $\psi_n(\rho)$ for the first three states of the exciton are given. (c) Schematic representation of 1s and 2s excitons and of the lines of the field in an inhomogeneous dielectric medium. (Adapted from Ref. [27].)

the binding energy and spatial size of the exciton that are in agreement with those obtained in the effective mass approximation. The model based on equation (23) does not take into account the peculiarities of the electronic band structure connected with the nonparabolicity of the electronic spectrum and symmetry of the crystal lattice either. These special features, although only weakly influencing the binding energy of the exciton, determine the fine structure of exciton states and can be taken into account in terms of the atomistic methods and multiband **kp**-model.

3.3 Fine structure of exciton energy levels

The selection rules for optical transitions with the participation of excitons, and also the fine structure of exciton energy levels and the mixing of different exciton states, can conveniently be analyzed using methods of symmetry analysis. To this end, let us establish transformation rules of the complete wave function of an electron–hole pair in a crystal (22) upon transformations of the symmetry group D_{3h} that describes the point symmetry of a monolayer.[2] The function $\Psi_X(\boldsymbol{\rho}_e, \boldsymbol{\rho}_h)$ is transformed according to the reducible representation

$$\mathcal{D}_X = \mathcal{D}_r \times \mathcal{D}_e \times \mathcal{D}_h \tag{28}$$

equal to the product of representations that describe the transformations of the envelope of function $\mathcal{D}_r$ and of the Bloch functions $\mathcal{D}_e$ and $\mathcal{D}_h$ of an electron and of a hole. In the group D_{3h}, any basis function of coordinates $\boldsymbol{\rho} = (x, y)$ in the plane of the monolayer is transformed either according to the one-dimensional representation $\mathcal{D}_r = \Gamma_1$ (invariant) or according to the two-dimensional representation Γ_6 (x, y components of the vector) in the notations used in book [34]. Thus, the envelope function $\psi(\boldsymbol{\rho})$ of the relative motion can have either s-type (Γ_1) or p-type (Γ_6) symmetry. The other envelope functions, which correspond to the projections of the angular momentum $l_z > 1$ onto the normal to the crystal, are transformed according to reducible representations [69]. In this section, we will analyze the fine structure of the exciton 1s states, which are characterized by an invariant envelope $\psi(\boldsymbol{\rho})$. The fine structure of the spectrum and the mixing of excitons with envelopes of different symmetries is analyzed in Section 3.4. The effects connected with the propagation of an exciton in the plane of the monolayer are discussed further in this section and in Section 4.2.

Subsequently, we will be interested only in the A-series excitons, formed with the participation of a hole in the upper spin subband of the valence band (see Fig. 2). Notice that the

[2] Although the excitons consist of electrons and holes at the $\mathbf{K}_\pm$ points on the boundary of the Brillouin zone, the wave vector of the center of masses of excitons excited in optical experiments is small in comparison with the lattice parameter. This makes it possible to consider excitons only with the wave vectors of the center of masses near the center of the Brillouin zone and, correspondingly, to use for the analysis of their fine structure the symmetry of a monolayer rather than of an individual valley.

fine structure of the B excitons, in which the hole occupies the lower spin subband, is similar to the structure of the A excitons, and the mixing of A and B excitons can be, as a rule, ignored because of a substantial, ~ 100 meV, spin splitting of the valence band. The Bloch functions of the top of the valence band are transformed according to the irreducible spinor representations Γ_7 (valley $\mathbf{K}_+$) and Γ_8 (valley $\mathbf{K}_-$) of the symmetry group C_{3h} of the wave vector at the $\mathbf{K}_\pm$ points, which correspond to the two-dimensional spinor representation Γ_7 of the group D_{3h}. In contrast to the valence band, in the conduction band it is necessary to take into account two closest-in-energy Kramers doublets $(\uparrow\mathbf{K}_+, \downarrow\mathbf{K}_-)$ and $(\downarrow\mathbf{K}_+, \uparrow\mathbf{K}_-)$. The first of these doublets, in which the spin of the electron in the conduction band (lower subbands in the materials based on Mo, and upper subbands in the W-based materials) coincides with the spin of the electron at the top of the valence band in the same valley, corresponds to the representations Γ_{11} and Γ_{12} of the group C_{3h}, and transforms according to the representation Γ_9 of the group D_{3h}. The second doublet, in which the spins of the electron in the valence band and in the conduction band in the same valley are opposite, corresponds to the representations Γ_9 and Γ_{10} of the group C_{3h} and is transformed according to the representation Γ_8 of the group D_{3h} [70]. The excitons formed with the participation of the states of the conduction band $(\uparrow\mathbf{K}_+, \downarrow\mathbf{K}_-)$ are transformed according to the reducible representation

$$\mathcal{D}_{\mathrm{X},\parallel} = \Gamma_1 \times \Gamma_7 \times \Gamma_9 = \Gamma_5 + \Gamma_6\,. \tag{29}$$

Hence, it can be seen that the quadruplet of the exciton states formed from the Bloch functions of the top of the valence band and of the lower (upper) subbands of the conduction band in $\mathrm{Mo}X_2$ ($\mathrm{W}X_2$) monolayers is split into two doublets, one of which is optically active for light polarization in the plane of the monolayer (Γ_6), and the other inactive in the electric dipole approximation (Γ_5). The optically active excitons Γ_6 are direct in the momentum space in the sense that an electron in the conduction band and the unoccupied site in the valence band are located in the same valley, whereas the Γ_5 excitons are indirect (Fig. 8).

The four exciton states formed with the participation of the states of the conduction band $(\downarrow\mathbf{K}_+, \uparrow\mathbf{K}_-)$ are transformed according to the rule

$$\mathcal{D}_{\mathrm{X},\uparrow\downarrow} = \Gamma_1 \times \Gamma_7 \times \Gamma_8 = \Gamma_3 + \Gamma_4 + \Gamma_6'\,. \tag{30}$$

Here, Γ_6' is a representation that is equivalent to Γ_6. According to formula (30), this quadruplet is split into one forbidden state Γ_3, one state Γ_4, which is active in the z-polarization of light along the normal to the layer, and a doublet of indirect excitons Γ_6', which are active in light polarization in the plane of the monolayer in processes with the participation of intervalley phonons which are transformed according to the invariant representation Γ_1. The schemes of energy levels of 1s excitons and corresponding phononless optical transitions are represented in Fig. 8.

Exciton states whose wave functions are transformed according to different irreducible representations of the group D_{3h} are generally split in energy. The microscopic nature of these splittings is determined by three contributions. First, the single-particle spin splitting Δ_c of the conduction band (see Fig. 8) leads to the splitting of quadruplets (29) and (30). Second, the small difference in

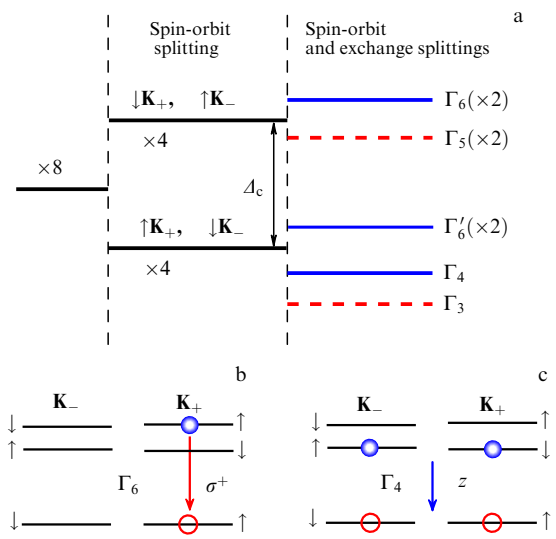

Figure 8. (Color online.) Schematic representation of the fine structure of the spectrum of 1s excitons and corresponding optical transitions in MX_2 monolayers. (a) The eightfold degenerate level is split into sublevels that correspond to different representations of the group D_{3h}. The optically active states are shown by solid lines. (b) The emission of a circularly polarized photon (in the plane of the monolayer) upon recombination of the Γ_6 exciton. The analogous transition in σ^- polarization occurs with the participation of an electron in the $\mathbf{K}_-$ valley. (c) The emission of the z-polarized photon upon recombination of the Γ_4 exciton, which is a symmetric linear combination of direct excitons with the electrons $(\downarrow\mathbf{K}_+, \uparrow\mathbf{K}_-)$. The linear combination orthogonal to it (representation Γ_3) is optically inactive. In Figs 8b and 8c, the unfilled circles denote the empty states in the valence band.

the effective masses of electrons in the upper and lower subbands of the conduction band, which appears in the **kp**-model when taking into account the spin-orbit splitting of the valence band, leads to a difference in the binding energies of the corresponding excitons on the order of $(\Delta_v/E_g)E_b$, where E_b is the binding energy of an exciton. The ratio Δ_v/E_g varies greatly for different materials: for MoS_2, it is ≈ 0.06.

The third contribution to the fine structure of exciton states is connected with the exchange interaction between the electron and hole [61, 63, 64, 71], which is the consequence of the antisymmetrization of the multiparticle wave function of the excited electron in the conduction band and of the remaining electrons in the Fermi sea of electrons. The exchange interaction leads to additional contributions to the energy of an electron–hole pair, which depend on the spin and valley indices of charge carriers and is ignored in the hydrogen-like Schrödinger equation (23). The microscopic calculation of the shifts of the exciton energy levels due to the exchange interaction is based on the knowledge of the Bloch functions of states in the conduction band and in the valence band and must be carried out within the framework of the atomistic methods. Calculations done within the framework of the DFT method [72, 73] show that the short-range exchange interaction of an electron and hole increases the energy of bright states Γ_6 in comparison with the dark states Γ_4 in materials such as MoS_2, $MoSe_2$, $MoTe_2$, WS_2, and WSe_2. Therefore, in Mo-based structures, the single-particle and exchange contributions can partially compensate for each other; in such systems, it is expected that the states optically active for light polarization in the plane of the monolayer and along the normal to it will be

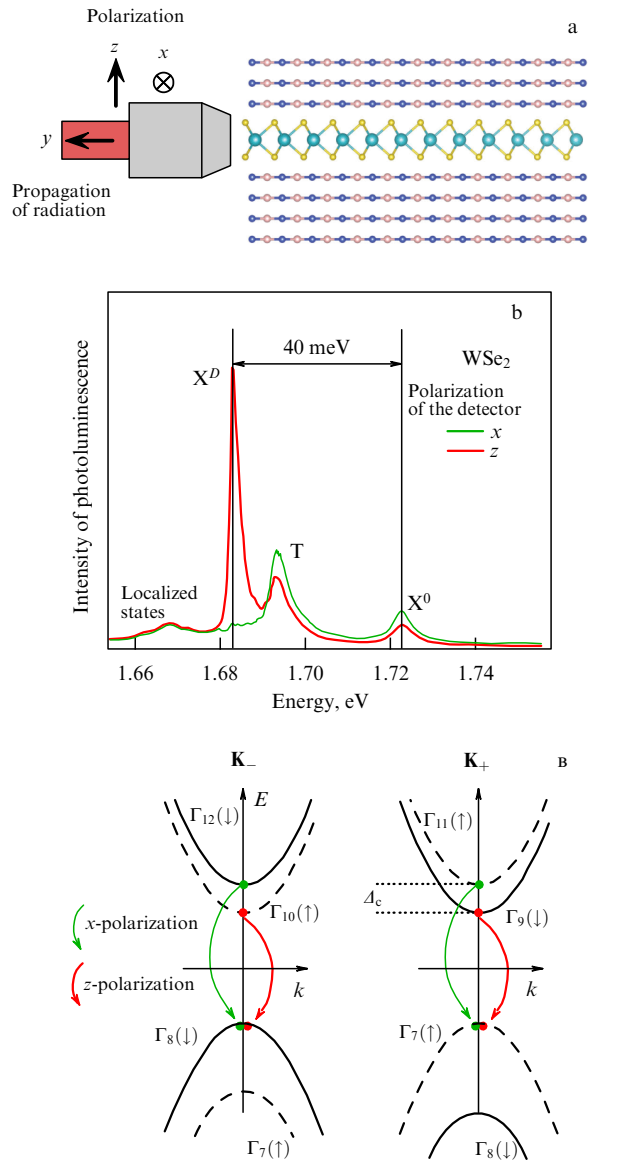

Figure 9. (Color online.) (a) Illustration of the experiment on the detection of the emission of excitons, polarized in the plane of the monolayer (x- polarization) and along the normal (z-polarization). Light propagates in the plane of the layered structure hBN/WSe_2 monolayer/hBN at $T = 13$ K, where hBN is hexagonal boron nitride. (b) The spectrum of the photoluminescence measured in paper [70], in appropriate polarizations. (c) Scheme of bands and transitions. The bands are designated according to the irreducible representations of the group C_{3h}, which correspond to the $\mathbf{K}_{\pm}$ points, and Δ_c is the spin splitting of the conduction band.

close in energy [72]. On the contrary, in W-based structures, both contributions have the same sign, and the splitting between the Γ_6 and Γ_4 excitons proves to be significant [72, 74]. This is confirmed by both indirect experimental data on the temperature dependence of the intensity of luminescence [75–77] and direct measurements of the spectra of photoluminescence for the light that propagates in the plane of the monolayer [70].

The experimental data presented in Fig. 9b demonstrate the splitting between the exciton states optically active for light polarization in the plane of the structure (peak X^0) and along the normal to it (peak X^D), whose value in the WSe_2 monolayers is on the order of 40 meV. It should be noted that in experiments the transition X^0 is also observed in the case of z-polarization, which is explained, apparently, by the finite aperture of the objective that registers the emission [70]. Microscopically, the optical activity of the state Γ_4 is connected with the spin-orbit mixing of the states of the conduction band and valence band with the states of the remote bands odd with respect to the reflection: $z \to -z$ [70, 78]. Estimates performed in the **kp**-model [70] and within the framework of the DFT method [72] give the ratio of the oscillator strengths for the states X^D and X^0 on the order of 10^{-4} to 10^{-2}. Measurement of the radiation decay of the Γ_4-symmetry states is an urgent experimental issue.

Let us now move to the analysis of the fine structure of the energy spectrum of a radiative doublet, the pair of Γ_6-symmetry states optically active in the x- and y-polarizations or σ^+ and σ^- in the plane of the layer. Specifically, it is precisely this doublet that plays the determining role in the optical properties of the MX_2 monolayers. The analysis made in Refs [63, 79–81] shows that the fine structure of the energy spectrum of the radiative doublet is similar to the fine structure of optically active exciton states in quantum wells on the basis of the III–V and II–VI semiconductors [61, 82–84]. Indeed, the direct product $\Gamma_6 \times \Gamma_6 = \Gamma_1 + \Gamma_2 + \Gamma_6$ contains, apart from the invariant representation Γ_1 and the representation Γ_2, according to which the z-component of the magnetic field is transformed, the two-dimensional representation Γ_6, according to which the quadratic components of the wave vector $\mathbf{K}$ of the center of masses of the exciton are transformed in the plane of the structures, $K_x^2 - K_y^2$ and $2K_xK_y$. Therefore, the effective Hamiltonian of the radiative doublet in the basis of the states active in the right-hand and left-hand circular polarizations takes on the form

$$\mathcal{H}_{\Gamma_6}(\mathbf{K}) = \frac{\hbar^2 K^2}{2M}\,\hat{I} + \begin{pmatrix} 0 & \alpha(K_x - \mathrm{i}K_y)^2 \\ \alpha(K_x + \mathrm{i}K_y)^2 & 0 \end{pmatrix} = \frac{\hbar^2 K^2}{2M}\,\hat{I} + \frac{\hbar}{2}(\mathbf{\Omega}_{\mathbf{K}}\boldsymbol{\sigma})\,. \tag{31}$$

Here, the reference point of the energy corresponds to the energy of the doublet at $\mathbf{K} = 0$, $M = m_e + m_h$ is the effective mass of the translational motion of the exciton in the plane of the monolayer, $\hat{I}$ is the two-row unit matrix, and $\alpha \equiv \alpha(K)$ is the mixing parameter. In the representation of the exciton pseudospin, when the state active in the σ^+ (σ^-) polarization is associated with the projection of the pseudospin $S_z = +1/2$ ($S_z = -1/2$) onto the normal to the structure, the effective Hamiltonian (31) can be written out in a form similar to the spin-orbital Hamiltonian for electrons [61, 85] [see the second equality in formula (31)]. In this Hamiltonian, $\boldsymbol{\sigma} = (\sigma_x, \sigma_y)$ is the vector comprising Pauli matrices, and $\mathbf{\Omega}_{\mathbf{K}}$ is the effective frequency of the pseudospin precession, which is sometimes called the effective magnetic field with nonzero components $\hbar\Omega_{\mathbf{K},x} = 2\alpha K^2 \cos(2\vartheta)$ and $\hbar\Omega_{\mathbf{K},y} = 2\alpha K^2 \sin(2\vartheta)$, where ϑ is the angle between $\mathbf{K}$ and the x-axis in the plane of the structure. The effective field is described by the second angular harmonics of the wave vector $\mathbf{K}$, since the transfer of the projection of moment 2 is necessary for a change in the circular polarization from σ^+ to σ^-. The operation of the time inversion does not reverse the sign of matrices σ_x and σ_y that act on the pseudospin of the exciton; therefore, the Hamiltonian is invariant relative to this conversion. The splitting between the eigenstates of Hamiltonian (31) is $\hbar\Omega_K = 2\alpha K^2$, and the eigenmodes are linearly polarized along $\mathbf{K}$ (longitudinal exciton L) and across $\mathbf{K}$ (transverse

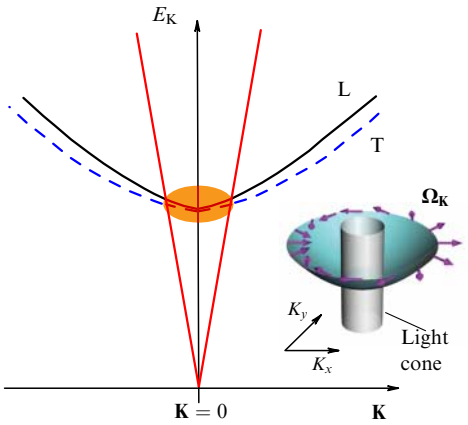

Figure 10. (Color online.) Schematic illustration of the dispersion of an exciton and splitting of a radiation doublet into linearly polarized states; point $\mathbf{K} = 0$ corresponds to the center of the Brillouin zone for the exciton. The states inside the light cone are marked by red. In the inset, the orientation of the effective field $\mathbf{\Omega_K}$ is shown as a function of the direction of the wave vector $\mathbf{K}$ of the exciton.

exciton T). The splitting of the exciton states and the orientation of the field $\mathbf{\Omega_K}$ are illustrated in Fig. 10.

Microscopically, the parameter $\alpha(K)$ in formula (31) is determined by the long-range exchange interaction between an electron and hole [61, 62, 71]. It can be calculated both within the framework of the **kp** perturbation theory, which takes into account the mixing of the states of the conduction and valence bands in the calculation of the matrix element of the Coulomb interaction, and within the framework of the electrodynamic approach to the joint solution of the Maxwell equation for the electromagnetic field generated by the exciton and for its dielectric polarization [63, 79]. If we assume that the coefficient of the reflection of light from the monolayer far from the exciton resonance is equal to zero, then, within the framework of the electrodynamic approach to the parameter $\alpha(K)$ in the limit when the wave vector K of the exciton is much more than the wave vector q of light at the frequency of the exciton resonance, we have

$$\alpha(K) = \frac{\hbar\Gamma_0}{2Kq}\,, \tag{32}$$

where Γ_0 is the radiative decay rate of the exciton. As can be seen from formulas (31) and (32), the longitudinal–transverse splitting of the exciton states in the region $K \gg q$ grows linearly with increasing K. A rigorous analysis [63, 79, 84], which takes into account the retardation of the Coulomb interaction, shows that expressions (31) and (32) are applicable only for states of the exciton outside the light cone, $K \gg q$. The states of a two-dimensional exciton for $K \leqslant q$ decay due to the emission of electromagnetic waves, and it makes no sense to speak about a shift in the energy levels in this case. In this case, the long-range exchange interaction leads to a polarization-dependent renormalization of the exciton radiative lifetime.

3.4 Mixing of exciton states with different parities

Let us now go on to effects caused by the absence of the center of space inversion in the point group D_{3h}. In order to analyze the fine structure of exciton states and the mixing of excitons with different parities, we will concentrate on the states with two-particle Bloch functions $u_{\mathrm{c},\mathbf{K}_\pm}(\boldsymbol{\rho}_\mathrm{e})\tilde{u}_{\mathrm{v},\mathbf{K}_\mp}(\boldsymbol{\rho}_\mathrm{h})$ [cf. formula (22)], which constitute the basis of the representation Γ_6. As was shown in Section 3.3, these states are optically active for light polarization in the plane of the monolayer. Let us now analyze the symmetry of exciton p-states, i.e., the excitons, the envelope wave function of which is also transformed according to the representation Γ_6. According to formula (28), the complete wave function of the p-exciton is transformed according to the reducible representation

$$\mathcal{D}_\mathrm{p} = \Gamma_6 \times \Gamma_6 = \Gamma_1 + \Gamma_2 + \Gamma_6\,. \tag{33}$$

It follows from expression (33) that, taking into account the point symmetry of the monolayer, the group of four p-states is split into two nondegenerate sublevels (representations Γ_1, Γ_2) and into a doubly degenerate sublevel Γ_6. The wave functions of these states can be represented in the following form [69]:

$$\Gamma_1\colon\ \psi_{p_x}\mathcal{U}_x + \psi_{p_y}\mathcal{U}_y\,, \tag{34a}$$

$$\Gamma_2\colon\ \psi_{p_x}\mathcal{U}_y - \psi_{p_y}\mathcal{U}_x\,, \tag{34b}$$

$$\Gamma_6\,(1)\ \left[\Gamma_6\,(x)\right]\colon\ \psi_{p_x}\mathcal{U}_y + \psi_{p_y}\mathcal{U}_x\,, \tag{34c}$$

$$\Gamma_6\,(2)\ \left[\Gamma_6\,(y)\right]\colon\ \psi_{p_x}\mathcal{U}_x - \psi_{p_y}\mathcal{U}_y\,. \tag{34d}$$

Here, we omitted the normalization factors and introduced the following notations: ψ_{p_x}, ψ_{p_y} are the envelopes that are transformed as the x and y coordinates in the point group D_{3h}, and

$$\mathcal{U}_x = -\frac{1}{\sqrt{2}}\left[u_{\mathrm{c},\mathbf{K}_+}(\boldsymbol{\rho}_\mathrm{e})\tilde{u}_{\mathrm{v},\mathbf{K}_-}(\boldsymbol{\rho}_\mathrm{h}) - u_{\mathrm{c},\mathbf{K}_-}(\boldsymbol{\rho}_\mathrm{e})\tilde{u}_{\mathrm{v},\mathbf{K}_+}(\boldsymbol{\rho}_\mathrm{h})\right], \tag{35a}$$

$$\mathcal{U}_y = \frac{1}{\sqrt{2}}\left[u_{\mathrm{c},\mathbf{K}_+}(\boldsymbol{\rho}_\mathrm{e})\tilde{u}_{\mathrm{v},\mathbf{K}_-}(\boldsymbol{\rho}_\mathrm{h}) + u_{\mathrm{c},\mathbf{K}_-}(\boldsymbol{\rho}_\mathrm{e})\tilde{u}_{\mathrm{v},\mathbf{K}_+}(\boldsymbol{\rho}_\mathrm{h})\right] \tag{35b}$$

are the linear combinations of the Bloch functions of the excitons. The basis functions $\Gamma_6\,(1)$ and $\Gamma_6\,(2)$ are transformed in the group D_{3h} as the x and y components of the vectors, respectively, and, therefore, the corresponding states are optically active in x- and y-polarizations. The basis functions (34) can be presented in an alternative form, going over to the basis with a given z-component of the angular momentum $l_z = \pm 1$. Then, the basis functions of the representations Γ_1 (Γ_2) are $\psi_{p_{+1}}\mathcal{U}_{-1} \pm \psi_{p_{-1}}\mathcal{U}_{+1}$, and the basis of the two-dimensional representation Γ_6 are the functions $\psi_{p_{+1}}\mathcal{U}_{+1}$, $\psi_{p_{-1}}\mathcal{U}_{-1}$, where $\psi_{p_{\pm 1}} \propto \psi_{p_x} \pm \mathrm{i}\psi_{p_y}$ and $\mathcal{U}_{\pm 1} = u_{\mathrm{c},\mathbf{K}_\pm}(\boldsymbol{\rho}_\mathrm{e})\tilde{u}_{\mathrm{v},\mathbf{K}_\mp}(\boldsymbol{\rho}_\mathrm{h})$.

The states which are transformed according to different irreducible representations of the point symmetry group of the system can be split. In particular, the splitting of the 2p-excitons that are transformed according to the representation Γ_6 and to the reducible representation $\Gamma_1 + \Gamma_2$ was discussed in Refs [68, 86–88]. The intravalley functions $\psi_{p_{+1}}\mathcal{U}_{-1}$ and $\psi_{p_{-1}}\mathcal{U}_{+1}$ can be chosen as the basis of the reducible representation $\Gamma_1 + \Gamma_2$. Then, the splitting can be obtained within the framework of the effective two-band Hamiltonian (3) by taking into account the **kp** interaction in the conduction band and in the valence band. It turns out that in this valley the states with different projections of the moment $l_z = \pm 1$, for example, the states $\psi_{p_{-1}}\mathcal{U}_{+1}$ and $\psi_{p_{+1}}\mathcal{U}_{+1}$, become split. In this case, because of the symmetry relative to the time inversion, the pairs of states in the different valleys, $\psi_{p_{-1}}\mathcal{U}_{+1}$ and $\psi_{p_{+1}}\mathcal{U}_{-1}$, as well as $\psi_{p_{+1}}\mathcal{U}_{+1}$

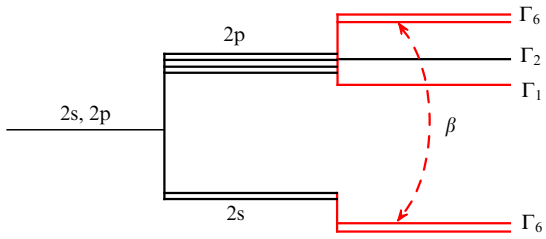

Figure 11. (Color online.) Illustration of exciton 2s- and 2p-states whose Bloch functions are transformed according to the representation Γ_6 of the group D_{3h} [see formula (35)]. The magnitudes and the signs of splittings are selected arbitrarily for illustrative purposes.

and $\psi_{p_{-1}}\mathcal{U}_{-1}$, have the same energy. The estimate of this intravalley splitting for the 2p-exciton is to an order of magnitude E_{2p}^2/E_g.

It also follows from formula (34) that the doublet $\Gamma_1+\Gamma_2$ can be split into two nondegenerate sublevels. Moreover, the pair of states Γ_6 generated by p-excitons has the same symmetry as the doublet Γ_6 with the envelopes of the s-symmetry [cf. formula (29)]. This indicates that the p- and s-states of excitons can be mixed up in the TMD monolayers. An illustration of the exciton states obtained on the basis of group-theoretical analysis is given in Fig. 11, where, as an example, the close-in-energy 2s and 2p states with Bloch functions (35) are examined.

Let us analyze in more detail the mixing of exciton s- and p-states. It follows from expression (34) that the $\psi_{p_x}\mathcal{U}_x-\psi_{p_y}\mathcal{U}_y$ state of the p-exciton is mixed with the $\psi_s\mathcal{U}_y$ state of the s-exciton, and the $\psi_{p_x}\mathcal{U}_y+\psi_{p_y}\mathcal{U}_x$ state is mixed with $\psi_s\mathcal{U}_x$. In the basis which is characterized by a given value of l_z, the following states are mixed [69]:

$$\psi_{p_{+1}}\mathcal{U}_{+1}\leftrightarrow\psi_s\mathcal{U}_{-1}\,,\qquad \psi_{p_{-1}}\mathcal{U}_{-1}\leftrightarrow\psi_s\mathcal{U}_{+1}\,. \tag{36}$$

If for each state we introduce the value of the total projection of the angular momentum, which includes the orbital angular momentum of the exciton envelope function and the projection ±1 of the angular momentum of Bloch functions, then, as can be seen from formula (36), there are mixed states, whose total momentum differs by ±3. Thus, the mixing of states according to Eqn (36) is a consequence of the trigonal symmetry of the group D_{3h}, namely, of the existence of a three-fold axis of rotation.

For the close-in-energy 2s and 2p levels, the effective Hamiltonian which describes the mixing of exciton states can be written out as follows:

$$\mathcal{H}_{2s-2p}=\begin{pmatrix} E_{2s} & 0 & \beta & 0\\ 0 & E_{2s} & 0 & \beta\\ \beta & 0 & E_{2p}^{(\Gamma_6)} & 0\\ 0 & \beta & 0 & E_{2p}^{(\Gamma_6)}\end{pmatrix}. \tag{37}$$

Here, the order of the basis functions is the following: 2s; $\Gamma_6(1)$, 2s; $\Gamma_6(2)$, 2p; $\Gamma_6(1)$, 2p; $\Gamma_6(2)$; the energies of states without taking into account s–p mixing, but taking into account, for example, the lifting of the accidental Coulomb degeneracy (see Fig. 6) are given on the diagonal of the matrix, and β is the mixing parameter.

In the microscopic approach, the mixing of exciton s- and p-states in the TMD monolayers is caused by the combination of the **kp**-admixture to the Bloch functions $u_{c,\mathbf{K}_\pm}(\boldsymbol{\rho}_e)$, $\tilde{u}_{v,\mathbf{K}_\mp}(\boldsymbol{\rho}_h)$ of the states from the remote bands [c + 2 and v − 3 in terms of the Hamiltonian $\mathcal{H}_{4,\pm}$; see formulas (5) and (6)] and of the exchange interaction between an electron and hole, which ensures the intervalley transfer of charge carriers. Estimates made within the framework of the microscopic theory [69] give for the constant β the values in the range from ~ 0.1 to ~ 1 meV, depending on the material and on the parametrization of the **kp** Hamiltonian.

The states of the p-excitons, whose wave functions are transformed according to the representation Γ_6, are optically active for light polarization in the plane of the monolayer. In this case, as can be seen from formula (36), the states with the $\psi_{p_{\pm1}}$ envelopes are active in $\sigma^\mp$-polarizations. The nonzero oscillator strength of the p-excitons is due to two factors. First, this is the mixing of 2p and 2s states, which is proportional to the parameter β. Second, as was shown in formulas (6) and (7), the matrix element of the momentum operator between the Bloch functions of the c and v bands contains contributions linear in the wave vector **k**, which are related to the mixing with remote bands in Hamiltonian (5):

$$\begin{aligned} p_{cv,x}^{\pm}&=\pm\frac{m_0}{\hbar}\,\gamma_3(1-Ak_\mp)\,,\\ p_{cv,y}^{\pm}&=\mathrm{i}\,\frac{m_0}{\hbar}\,\gamma_3(1+Ak_\mp)\,. \end{aligned} \tag{38}$$

Here, the superscripts $\pm$ refer to the valleys in which the matrix elements are considered. Taking into account these two factors, the rate of the radiative recombination of 2p-excitons takes on the following form:

$$\Gamma_{0,2p}=2\pi\alpha\,\frac{\gamma_3^2A^2\left|\psi'_{2p}(0)\right|^2}{\hbar\left(E_g-|E_{2p}|\right)}+\frac{2\pi\alpha\beta^2}{(E_{2s}-E_{2p})^2}\,\frac{\gamma_3^2\left|\psi_{2s}(0)\right|^2}{\hbar\left(E_g-|E_{2p}|\right)}\,, \tag{39}$$

where α is the fine-structure constant, and the following designation was introduced:

$$\psi'_{2p}(\rho)=\left(\frac{\partial}{\partial x}-\mathrm{i}\,\frac{\partial}{\partial y}\right)\psi_{2,p_{+1}}=\left(\frac{\partial}{\partial x}+\mathrm{i}\,\frac{\partial}{\partial y}\right)\psi_{2,p_{-1}}\,. \tag{40}$$

The ratio of $\Gamma_{0,2p}$ to the rate of the radiative recombination of 2s-excitons is to an order of magnitude A^2/a^2, where a is the characteristic size of the exciton wave function, for the first term in (39), and to $\beta^2/(E_{2s}-E_{2p})^2$ for the second term. The estimates made in Ref. [69] show that these ratios are comparable in magnitude.

The described mixing of exciton states of different parities appears to be due to the low symmetry of the MX_2 monolayer. Notice that the presence of a disorder, which leads to a local reduction in the symmetry, can also lead to mixing of the exciton states with different parities [89].

3.5 Charged excitons (trions)

When free charge carriers are present in the system, the electron–hole pair can become bound to a resident electron or hole and form a three-particle complex — a trion, or charged exciton. There are X^+ and X^- trions, consisting of two holes and one electron and one hole and two electrons, respectively. These complexes are similar to hydrogen-like ions H_2^+ and H^-. In bulk semiconductors, the binding energy of trions is very small [90]; upon reducing the dimensionality of the system and upon passage from the bulk material to two-dimensional systems — quantum wells — the role of the Coulomb interaction increases [91]. This led to the detection

of trions in quantum wells on the basis of semiconducting II–VI and III–V compounds in the 1990s, and to their subsequent active experimental and theoretical studies [92, 93]. Nevertheless, the binding energies of the trion are rather small in widely investigated semiconductor nanosystems and are, as a rule, on the order of 1/10 of the binding energy of the exciton [94, 95], i.e., units of millielectron-volts.

In TMD monolayers, a significant increase in the role of Coulomb attraction between the electrons and holes entailed a considerable increase in the binding energy of trions. Positively and negatively charged excitons with binding energies on the order of 30 meV were revealed in MX_2 monolayers [31, 96]. The wave function of a trion in a two-dimensional semiconductor can be represented in the form

$$\Psi_{i,j;k}(\boldsymbol{\rho}_a, \boldsymbol{\rho}_b, \boldsymbol{\rho}_c) = \exp(\mathrm{i}\mathbf{KR})\, \psi(\boldsymbol{\rho}_1, \boldsymbol{\rho}_2)\, \mathcal{U}_{ij}^{(2)}(\boldsymbol{\rho}_a, \boldsymbol{\rho}_b) u_k^{(1)}(\boldsymbol{\rho}_c)\,. \tag{41}$$

Here, the subscripts i and j stand for the states (a number of the band, spin, and valley index) of two identical charge carriers, namely, two electrons, e_1 and e_2, in an X^- trion, or two holes, h_1 and h_2, in an X^+ trion; the superscript k refers to an unpaired carrier; the subscripts a, b, and c similarly designate the coordinates of charge carriers; $\mathbf{R} = [m_a(\boldsymbol{\rho}_a + \boldsymbol{\rho}_b) + m_c\boldsymbol{\rho}_c]/M$ is the coordinate of the center of masses of a trion; $\mathbf{K}$ is the wave vector of its motion as a whole; m_a (m_c) is the mass of one of the identical (unpaired) charge carriers; $M = 2m_a + m_c$ is the total mass of the trion; $\psi(\boldsymbol{\rho}_1, \boldsymbol{\rho}_2)$ is the wave function of the relative motion of the charge carriers; $\boldsymbol{\rho}_{1,2} = \boldsymbol{\rho}_{a,b} - \boldsymbol{\rho}_c$ are the relative coordinates of the particles, and, finally, $\mathcal{U}_{ij}^{(2)}$ ($u_k^{(1)}$) is the Bloch function of a two-particle pair (unpaired particle). The normalization area, as before, is assumed to be equal to unity. It should be noted that, as in formula (22), the dependence of the Bloch functions of electrons and holes on the coordinate z is omitted. According to the general rules of quantum mechanics, wave function (41) should be antisymmetrized with respect to the permutations of identical particles a and b [97]. In the effective mass method, the binding energies of a trion and the envelope wave functions $\psi(\boldsymbol{\rho}_1, \boldsymbol{\rho}_2)$ are found by solving the Schrödinger equation with the effective Hamiltonian

$$\mathcal{H}_{\mathrm{tr}} = -\frac{\hbar^2}{2\mu}\left[\Delta_1 + \Delta_2 + \frac{2\sigma}{\sigma+1}\nabla_1\nabla_2\right] + V(\rho_1) + V(\rho_2) - V(|\boldsymbol{\rho}_1 - \boldsymbol{\rho}_2|)\,, \tag{42}$$

where Δ_l and ∇_l are the Laplace operator and gradient operator acting on the coordinates $\boldsymbol{\rho}_l$ ($l = 1, 2$), $\mu = m_e m_h/(m_e + m_h)$ is the reduced mass of an electron and hole, $\sigma = m_a/m_c$ is the ratio of the effective masses of one of the identical carriers to the mass of an unpaired carrier, e.g., $\sigma = m_e/m_h$ for the X^- trion, and $\sigma = m_h/m_e$ for the X^+ trion, and, finally, $V(\boldsymbol{\rho}) = -e\varphi_{2D}(\boldsymbol{\rho})$ is the effective potential energy of interaction (16). Calculations of the binding energy of trions in the monolayers of dichalcogenides of transition metals were performed in a number of studies [30, 32, 98, 99]. The analysis shows that for an electron and hole with close effective masses ($\sigma \approx 1$) only those trions whose envelope function is symmetrical (even) with respect to the permutations of two identical particles, $\psi(\boldsymbol{\rho}_1, \boldsymbol{\rho}_2) = \psi(\boldsymbol{\rho}_2, \boldsymbol{\rho}_1)$, prove to be stable [32, 100]. Taking into account the requirement of the antisymmetrization of the total wave function (41), we obtain for the Bloch function of the pair of identical particles the following expression

$$\mathcal{U}_{ij}^{(2)}(\boldsymbol{\rho}_a, \boldsymbol{\rho}_b) = \frac{1}{\sqrt{2}}\left[u_i(\boldsymbol{\rho}_a)u_j(\boldsymbol{\rho}_b) - u_i(\boldsymbol{\rho}_b)u_j(\boldsymbol{\rho}_a)\right]. \tag{43}$$

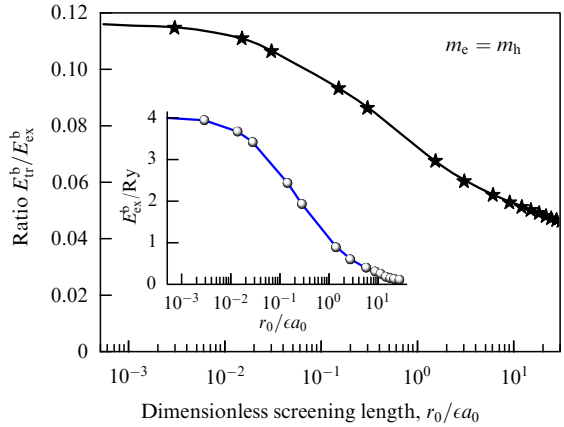

Figure 12. (Color online.) Ratio of the binding energy $E^{\mathrm{b}}_{\mathrm{tr}}$ of a trion to the binding energy $E^{\mathrm{b}}_{\mathrm{ex}}$ of an exciton depending on the screening parameter r_0 (17) with coinciding effective masses of the electron and hole, $\sigma = 1$. In the inset, the binding energy of the exciton depending on r_0 is shown (cf. Fig. 6). Units of the measurement of the energy and length are as follows: $\mathrm{Ry} = \mu e^4/2(\hbar\epsilon)^2$, and $a_0 = \epsilon\hbar^2/(\mu e^2)$. (Adapted from Ref. [32].)

To illustrate, Fig. 12 presents the numerical calculation (based on the variational method) of the ratio between the binding energies of a trion (difference between the energy of a trion and the exciton energy) and of an exciton with the coinciding effective masses of the electron and hole depending on the screening parameter r_0 in formula (17) [32]. In the case of $\sigma = 1$, the binding energies of X^- and X^+ trions coincide. In the limit $r_0 \to 0$ of the weak screening, the ratio of the binding energies of an exciton and trion tend to a constant value of ≈ 0.12; with increasing r_0, when the potential connecting the charged particles becomes weaker, the binding energy of trions decreases more rapidly than the binding energy of the exciton. For the parameters of WSe_2 monolayers, the calculation gives the binding energy of trions in the range of 20–30 meV, depending on the model involved and on the parameters of the dielectric environment.

Let us now analyze the fine structure of a trion energy spectrum. As in Section 3.3, we will limit ourselves to the hole states in the upper spin subbands of the valence band. In this case, there are four opportunities for the X^+ trion, which satisfy requirement (43): two holes are located in the states that are antisymmetric with respect to spins and valleys, and the unpaired electron occupies one of the four states (two spin and two valley states) in the conduction band. From this quadruplet, two states do not interact with radiation polarized in the plane of the MX_2 monolayer, but the two others are optically active in σ^+- and σ^--polarizations. The splitting between the doublets is determined mainly by the spin splitting of the conduction band. In the spectra of reflection, absorption, and luminescence, the X^+ trion manifests itself as a single line [32] (Fig. 13c), which is split into circularly polarized components in the magnetic field.

In comparison with the X^+ trion, the negatively charged exciton (X^-) exhibits a considerably richer fine structure [80, 101, 102]. The analysis made in Refs [32, 103] shows that there are 12 states of the X^- trion that satisfy the requirements of

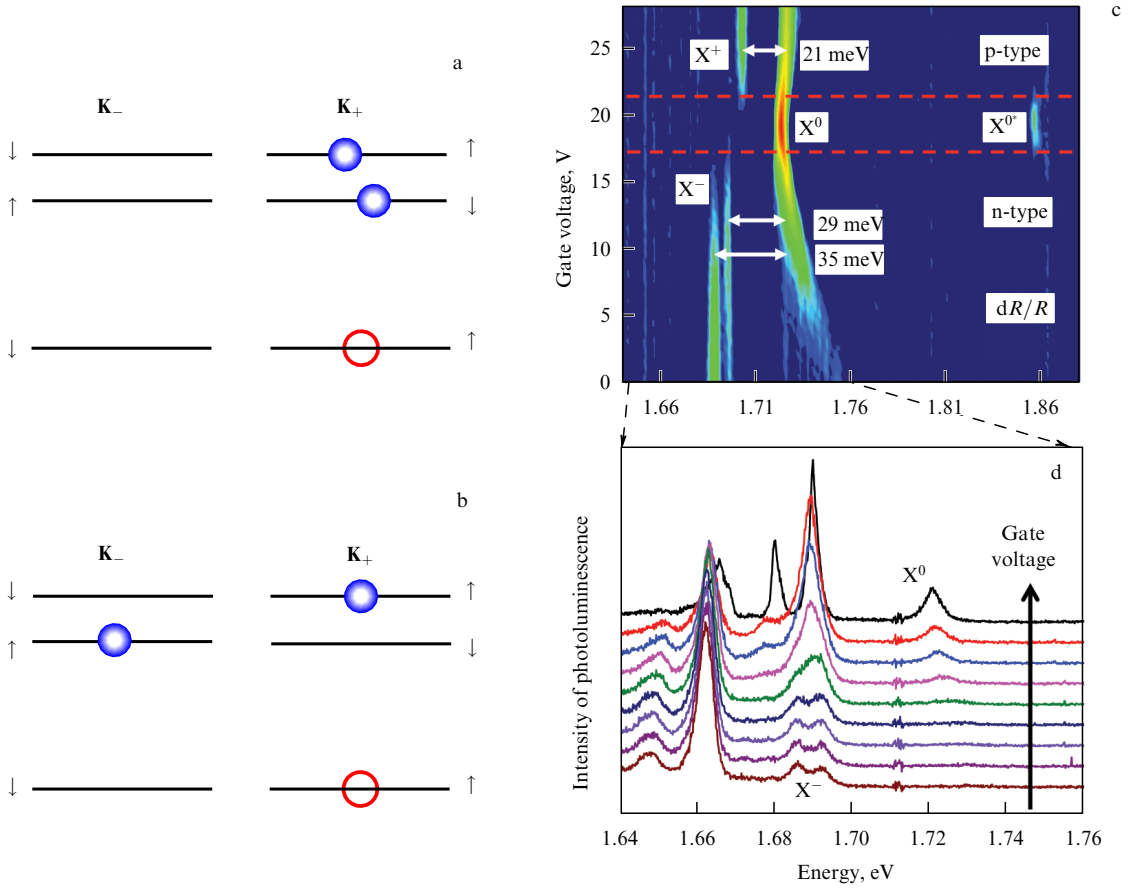

Figure 13. (Color online.) (a, b) Examples of optically active trion states in WSe_2. (c) First derivative of the reflection coefficient of the structure hBN/1ML WSe_2/hBN depending on the energy (abscissa) and on the gate voltage (ordinate). Regimes of p- and n-type doping are marked. (d) Evolution of the spectrum of photoluminescence upon transition from the neutral regime to the n-type doping with a change in the gate voltage. (Adapted from Ref. [32].)

antisymmetrization (43). In these states, the hole occupies the upper spin subband in one of two valleys, and for the pair of electrons there are six different options to occupy four states in the conduction band: two valley states, and two spin states. The energy positions of the trion energy levels and the selection rules in optical transitions connected with the excitation of a trion are determined by both the sign of the spin splitting Δ_c of the conduction band and the short-range exchange interaction between the electrons. For example, in WSe_2, where the spins of the electron in the upper subband of the valence band and in the lower subband of the conduction band are directed oppositely, the ground state of the trion, without taking into account the short-range corrections, is optically inactive in the light polarization in the plane of structure [32, 103].[3] Of the twelve states of the X^- trion, six are optically active for the light polarization in the plane of the monolayer: in these states, the electron and the hole have the identical projection of the spin in one valley (Figs 13a, 13b).

In the spectra of reflection (Fig. 13c) and luminescence (Fig. 13d) measured by Courtade et al. [32], two lines connected with 'intravalley' and 'intervalley' trions are observed in a zero magnetic field (cf. with Figs 13a, 13b). Notice that one more pair of optically active X^- trions, in which the electrons reside in the states $\uparrow\mathbf{K}^+$ and $\downarrow\mathbf{K}^-$, is not observed in the reflection experiments, since the level of doping of the sample investigated in Ref. [32] does not make it possible to excite such states upon absorbing a photon. The solution of the Schrödinger equation with Hamiltonian (42) gives an identical energy for all the above-discussed states of a given trion and, moreover, an identical energy of the X^+ and X^- trions at $\sigma = 1$. Therefore, splittings between the lines of the X^- trion and the difference in the spectral positions of the X^+ and X^- trions are connected mainly with the short-range electron–electron exchange interaction [32].

Notice in the conclusion of this section that in the structures that contain resident electrons correlations can arise between the photo-induced electron and hole and the Fermi sea of the resident charge carriers [104–107]. A detailed analysis of this type of correlations is an interesting experimental and theoretical problem which requires further study.

4. Magneto-optical effects and spin dynamics of excitons

One of the most powerful experimental methods for studying the fine structure of the energy spectrum is polarization-resolved optical spectroscopy. The wide range of effects that can be investigated by this method includes magneto-optical

[3] Due to the short-range exchange interaction, the ground state of the trion can mix with the higher-in-energy optically active state and thereby acquire a nonzero oscillator strength [32].

effects connected with a change in the spectra of luminescence, absorption, and reflection in the region of exciton resonances under the action of an external magnetic field, and also effects of the optical orientation of excitons, which appear upon excitation of monolayers of transition metal dichalcogenides by polarized light. In the two subsequent sections, we describe the most outstanding effects that relate to the above-indicated regions.

4.1 Zeeman effect

For the investigation of magneto-optical effects with the participation of Coulomb complexes — excitons and trions — it is necessary first to determine the Landé factors of free charge carriers in MX_2 monolayers. Among the wide range of theoretical approaches, the effective Hamiltonian method described in Section 2.3 makes it possible to most efficiently calculate the splitting of the spin sublevels of an electron in an external magnetic field — the Zeeman effect. Let us examine the Zeeman splitting of electrons in $\mathbf{K}_\pm$ valleys in a magnetic field directed along the normal to the monolayer, $\mathbf{B} = (0, 0, B_z)$. In the approximation linear in B_z, the Hamiltonian of an electron in a magnetic field contains spin and valley contributions described by the g-factors g_0 and g_{orb}:

$$\mathcal{H}_B = \frac{g_0}{2}\,\mu_{\text{B}} B_z \sigma_z + \frac{g_{\text{orb}}}{2}\,\mu_{\text{B}} B_z \tau_z\,. \tag{44}$$

Here, $\sigma_z = \pm 1$ for electrons with spin up and spin down, $\tau_z = \pm 1$ for electrons in the $\mathbf{K}_\pm$ valleys, respectively, and μ_{B} is the Bohr magneton. It follows from formula (44) that the energy level of a $\mathbf{K}_+$-electron with spin up ($\uparrow \mathbf{K}_+$) is shifted in the magnetic field by a value of $1/2(g_0 + g_{\text{orb}})\mu_{\text{B}} B_z$, whereas the state $\downarrow \mathbf{K}_-$ connected with it by time inversion is shifted by $-1/2(g_0 + g_{\text{orb}})\mu_{\text{B}} B_z$. Thus, the effective g-factors of the $\uparrow \mathbf{K}_+$-electron and $\downarrow \mathbf{K}_-$-electron can be defined as

$$g_{\text{c,v}}^{\uparrow \mathbf{K}+} \equiv g_{\text{c,v}} = g_0^{\text{c,v}} + g_{\text{orb}}^{\text{c,v}}\,, \qquad g_{\text{c,v}}^{\downarrow \mathbf{K}-} = -g_{\text{c,v}}^{\mathbf{K}+}\,, \tag{45}$$

where the super- and subscripts c and v denote an electron in the conduction band or in the valence band.

The valley contribution $g_{\text{orb}}^{\text{c,v}}$ is of an orbital nature, and it can be calculated within the framework of the effective **kp** Hamiltonian (5). For this, it is necessary to make a standard replacement $\mathbf{k} \to \mathbf{k} - (e/c\hbar)\mathbf{A}$ in the Hamiltonian, where $\mathbf{A}$ is the vector-potential of the magnetic field, and to calculate the shift in the extremum of the band in the second-order perturbation theory. As a result, we obtain [47]

$$\begin{aligned} g_{\text{orb}}^{\text{c}} &= \frac{4m_0}{\hbar^2}\left(-\frac{\gamma_5^2}{E_{\text{c}} - E_{\text{v}-3}} + \frac{\gamma_3^2}{E_{\text{c}} - E_{\text{v}}} - \frac{\gamma_6^2}{E_{\text{c}} - E_{\text{c}+2}}\right), \\ g_{\text{orb}}^{\text{v}} &= \frac{4m_0}{\hbar^2}\left(\frac{\gamma_2^2}{E_{\text{v}} - E_{\text{v}-3}} - \frac{\gamma_3^2}{E_{\text{v}} - E_{\text{c}}} + \frac{\gamma_4^2}{E_{\text{v}} - E_{\text{c}+2}}\right). \end{aligned} \tag{46}$$

The spin g-factor, $g_0^{\text{c,v}}$, involves two contributions: one from the g-factor of a free electron ($g_0 = 2$) and another small contribution connected with the spin-orbit interaction. The latter contribution can be estimated as $\sim g_{\text{orb}} \Delta_{\text{so}}/\Delta E_{ij} \ll g_{\text{orb}}$, where Δ_{so} is the spin-orbit splitting of the band, and ΔE_{ij} is the characteristic value of the energy gap between the bands.

In magneto-optical experiments, shifts in the lines of photoluminescence are observed for s-excitons optically active in σ^+- and σ^--polarizations in the plane of the layer (the corresponding states are transformed according to the two-dimensional representation Γ_6; see Section 3.3). The splitting of the σ^+- and σ^--polarized lines is equal to $\Delta_Z = g_{\text{X}^0}\mu_{\text{B}} B_z$, where g_{X^0} is the effective g-factor of the exciton, which, when disregarding the Coulomb interaction and the nonparabolicity of the bands, is equal to

$$g_{\text{X}^0} = g_{\text{c}} - g_{\text{v}}\,. \tag{47}$$

It should be noted that within the framework of the two-band approximation (3) the parameter g_{X^0} is equal to zero, since the quantities g_{c} and g_{v}, which are given by formulas (45) and (46) with the only nonzero parameter γ_3, coincide. The measured values of g_{X^0} in TMD monolayers vary in the range from $g_{\text{X}^0} \approx -2$ to $g_{\text{X}^0} \approx -4$ (for example, see Refs [47, 108–112]).

Thus, the nonzero value of g_{X^0} is connected with the admixture of other electron bands to the v and c bands [47]. In the model under consideration, the main contribution to g_{X^0} comes from the bands c + 2 and v − 3, which are taken into account in the four-band Hamiltonian (5) [45]. As was noted in Section 2.3, the parametrization of the **kp** Hamiltonian and, in particular, the parameters γ_2, γ_4, γ_5, and γ_6, can be obtained with the aid of an expansion of the tight binding Hamiltonian near the $\mathbf{K}_\pm$ points [see formula (9)]. The analysis performed in Ref. [45] shows that for a number of systems in this approach both the parameters of the tight binding method and the parameters of the **kp** Hamiltonian can be optimized in order to obtain substantial (~ 1) absolute values of the g-factor of an exciton (see Table 2). Further experimental and theoretical studies of magneto-optical effects on trions and on the localized exciton states in MX_2 monolayers will make it possible to ascertain the role of Coulomb interactions in the renormalization of the g-factor of individual charge carriers and electron–hole complexes.

4.2 Spin and valley dynamics of excitons

The presence of spin and valley degrees of freedom in the excitons in TMD monolayers is manifested especially vividly in experiments on the optical orientation and optical alignment of excitons [22–24, 47, 113–116]. In the absence of an external magnetic field, the excitation of MX_2 monolayers by circularly polarized light leads to a preferential population of one of two states of the radiative doublet: with the projection of the pseudospin $S_z = +1/2$ upon excitation by σ^+-polarized light, and with the projection of the pseudospin $S_z = -1/2$ upon excitation by σ^--polarized light (see Section 3.3). The absorption of the linearly polarized light leads to the excitation of coherent superpositions of the states with $S_z = \pm 1/2$, in which the valley states of the electron and hole become entangled [63, 79, 117].

The model description of the spin and valley dynamics of excitons can be conveniently carried out in the formalism of the pseudospin, presented above in application to the description of the fine structure of the energy spectrum of the radiative doublet. The pseudospin density matrix $\varrho_{\mathbf{K}}$ of the 2×2 dimension, which describes the states of the radiative doublet in the basis of $S_z = \pm 1/2$, can be written out in the form [63, 79]

$$\varrho_{\mathbf{K}} = n_{\mathbf{K}} \hat{I} + \mathbf{S}_{\mathbf{K}} \boldsymbol{\sigma}\,, \tag{48}$$

where $n_{\mathbf{K}} = \text{Tr}\,\{\varrho_{\mathbf{K}}/2\}$ is the spin-averaged distribution function of the excitons, and $\mathbf{S}_{\mathbf{K}} = \text{Tr}\,\{\varrho_{\mathbf{K}}\boldsymbol{\sigma}/2\}$ is the pseudospin. Its components describe the orientation of the microscopic dipole moment of excitons, in particular, S_z/n determining the degree of the circular polarization of the

excitons (in the literature, the term 'valley polarization' is also used, which emphasizes the chiral selection rules in the excitation of MX_2 monolayers), and the ratios S_x/n and S_y/n determining the degree of linear polarization of excitons in the (x, y) and (x', y') axes rotated with respect to each other by 45°. The components S_x and S_y determine the degree of alignment of the excitons [118] or, as also said, their valley coherence. The pseudospin vector $\mathbf{S_K}$ and the scalar $n_\mathbf{K}$ satisfy the system of kinetic equations [63, 79, 82, 119]

$$\frac{\partial \mathbf{S_K}}{\partial t} + \mathbf{S_K} \times \mathbf{\Omega_K} + \frac{\mathbf{S_K}}{\tau_0(\mathbf{K})} = \mathbf{Q}\{\mathbf{S_K}, n_\mathbf{K}\} + \mathbf{G}\,, \tag{49a}$$

$$\frac{\partial n_\mathbf{K}}{\partial t} + \frac{n_\mathbf{K}}{\tau_0(\mathbf{K})} = Q\{n_\mathbf{K}, \mathbf{S_K}\} + g\,, \tag{49b}$$

where the $\mathbf{\Omega_K}$ vector is defined in formula (31); the collision integrals $\mathbf{Q}\{\mathbf{S_K}, n_\mathbf{K}\}$ and $Q\{n_\mathbf{K}, \mathbf{S_K}\}$ describe the redistribution of excitons in the momentum space due to their interaction with defects, phonons, and each other; $\tau_0(\mathbf{K})$ is the exciton lifetime (which takes into account both the radiation and radiationless channels of recombination), and the quantities $\mathbf{G}$ and g describe the rates of generation of excitons due to, for example, photoexcitation or electrical injection. The common form of the collision integrals for the two-dimensional bosons is discussed in papers [120–123], and in the simplest case the collision integral $\mathbf{Q}\{\mathbf{S_K}, n_\mathbf{K}\}$ can be written out in the approximation of the relaxation time as follows:

$$\mathbf{Q}\{\mathbf{S_K}, n_\mathbf{K}\} = -\frac{\mathbf{S_K} - \overline{\mathbf{S_K}}}{\tau}\,, \tag{50}$$

where the over-bar designates averaging over the angle ϑ between the vector $\mathbf{K}$ and the axis in the monolayer plane, and τ is the time of relaxation of the anisotropic part of the distribution function. To describe the spatially inhomogeneous distribution of excitons, the left-hand sides of equations (49) should be supplemented with the gradient contributions $(\mathbf{v_K}\nabla)\mathbf{S_K}$ and $(\mathbf{v_K}\nabla)n_\mathbf{K}$, where $\mathbf{v_K} = \hbar\mathbf{K}/M$ is the exciton velocity in the $\mathbf{K}$ state.

Figure 14 presents experimental data (dots) on the relaxation time of the z-component of the pseudospin of excitons obtained by Zhu et al. [115] on a WSe_2 monolayer using the method of pump–probe time-resolved Kerr rotation. The optical orientation of excitons was created by a strong circularly polarized laser pulse, while the detection of the S_z dynamics was carried out using a weaker linearly polarized pulse by the rotation of the plane of polarization in the geometry for the reflection (spin Kerr effect) [115, 124]. In the experiment, a rapid acceleration of the spin relaxation of excitons with an increase in temperature was observed. Qualitatively, this effect is connected with an increase in the characteristic wave vectors of excitons and, correspondingly, in the absolute value of the effective field $\Omega_\mathbf{K}$ with an increase in temperature of the sample. In those cases where the inverse relaxation time τ^{-1} significantly exceeds the frequency of the pseudospin precession in the effective field $\Omega_\mathbf{K}$, for the rate of the spin/valley relaxation of excitons we have [63, 79, 115] (cf. Ref. [125])

$$\frac{1}{\tau_{\mathrm{s,v}}} = \langle \Omega_\mathbf{K}^2 \tau \rangle \propto \tau T\,, \tag{51}$$

where the angle brackets designate averaging over the Boltzmann distribution of excitons, and T is the temperature of the exciton gas, which is assumed to be equal to the lattice temperature. The calculation with the only adjustable parameter τ describes well the results of the experiment [115]. At low temperatures, the time of the spin/valley relaxation of excitons weakly depends on T; apparently, this is connected with the effects of exciton localization on the monolayer defects.

It should be noted that, at present, studies of the kinetic parameters of excitons are very sparse. In particular, the measured recombination times of excitons with small wave vectors (inside the light cone) are on the order of 1 ps [126, 127], which is in agreement with estimates made within the framework of the two-band **kp**-model [63, 79]. The lifetime of the entire ensemble of excitons is considerably longer and can reach several nanoseconds, since radiative recombination for dark exciton states (spin-forbidden states and states with $\mathbf{K}$ lying outside the light cone) is limited, apparently, by conversion into optically active states or by nonradiative processes (for example, by the Auger recombination, which, however, is suppressed in the case of small concentrations of excitons) [128–131]. The scattering time τ of excitons can vary greatly, depending on the origin of a sample and temperature, from units of picoseconds to ten femtoseconds [for the time on the order of 10 fs, generally speaking, the criterion of the applicability of kinetic equations (49) is violated] [132, 133].

Notice that a spin and valley orientation of resident charge carriers was observed in a number of recent experiments on the TMD monolayers [134–137].

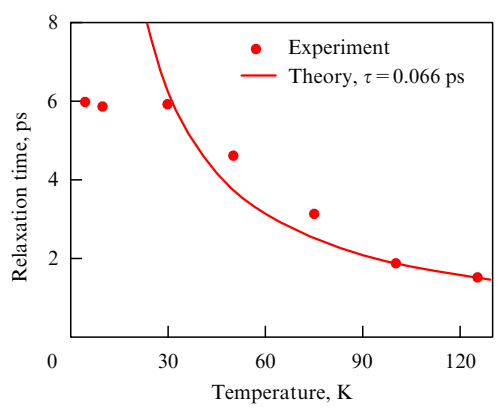

Figure 14. (Color online.) Temperature dependence of the measured (circles) and calculated (solid curve) time of the spin/valley relaxation of excitons depending on the lattice temperature in the WSe_2 monolayer. (Adapted from Ref. [115].)

5. Excitons in nonlinear optical effects

The investigation of the nonlinear optical and transport responses of semiconductors and of semiconductor nanosystems is a powerful tool for the study of the properties of energy spectra and kinetic processes [61, 138–141]. This section is devoted to a review of the basic effects showing themselves in the nonlinear optics based on excitons in TMD monolayers and of their connection with the fine structure of exciton states.

5.1 Two-photon absorption

One of the simplest nonlinear optical effects is two-photon absorption, in the course of which a semiconductor absorbs two photons and the crystal turns out to be in an excited state. Within the framework of the phenomenological approach,

the two-photon absorption can be attributed to the third-order nonlinear effects in terms of the complex amplitude $\mathbf{E}_\omega$ of the electromagnetic field incident onto the sample [138, 141]:

$$P_{\omega,i} = \chi^{(3)}_{ijkl} E_{\omega,j} E_{-\omega,k} E_{\omega,l} + \text{c.c.} \tag{52}$$

Here, the subscripts $i, j, k, l = x, y, z$ denote Cartesian components, $\chi^{(3)}_{ijkl}$ is the corresponding nonlinear susceptibility, and c.c. is the complex conjugate contribution; in this case, the dielectric polarization $\mathbf{P}_\omega$ and the electric field $\mathbf{E}_\omega$ are defined in the complex form according to

$$\mathbf{P} = \mathbf{P}_\omega \exp(-\mathrm{i}\omega t) + \mathbf{P}_{-\omega} \exp(\mathrm{i}\omega t)\,,$$
$$\mathbf{E} = \mathbf{E}_\omega \exp(-\mathrm{i}\omega t) + \mathbf{E}_{-\omega} \exp(\mathrm{i}\omega t)\,.$$

Below, we will ignore the effects of spatial dispersion, i.e., the presence of coordinate dependence of the electric field and polarization. In the exciton part of the spectrum, this is justified when the wave vector q of light is small in comparison with the inverse Bohr radius of the exciton and with the reciprocal lattice parameter, except, perhaps, a narrow region near the very resonance [56, 142].

Usually, exciton two-photon absorption in semiconductors is studied in the regime where the total energy $2\hbar\omega$ of the light quanta is close to the excitation energy of some exciton state. For the exciton state to be active in two-photon absorption, its wave function must transform as some quadratic combination of the fields $E_{\omega,i} E_{\omega,j}$. On the contrary, for single-photon absorption, the wave function of the exciton must transform as the $E_{\omega,i}$ component of the field vector. In centrosymmetrical crystals, this condition imposes the requirement of an alternative prohibition: any given state of an exciton is active either in the single-photon or in the two-photon process. In particular, it is the p-states of the exciton that are active in two-photon absorption [86, 143]. Their excitation occurs via a two-stage process, where states in the conduction band or in the valence band come out as intermediate states. The matrix element of the two-photon excitation of mp-excitons ($m = 2, 3, \ldots$) is calculated within the framework of the two-band model (3) and can be written out as follows [69, 143]:

$$M^{(2,\pm)}_{m\mathrm{p}} = \langle \Psi^{\pm}_{m\mathrm{p}} | \hat{V}^{(2)}_{\mathrm{ph}} | 0 \rangle = \left(\frac{e}{\omega}\right)^2 \left(\mp \frac{\mathrm{i}\gamma_3}{\hbar\omega\mu}\right) [\psi'_{m\mathrm{p}}(0)]^* E^2_{\sigma^\pm}\,. \tag{53}$$

Here, $|0\rangle$ denotes the ground state of the crystal, $\hat{V}^{(2)}_{\mathrm{ph}}$ is the operator of a two-photon transition, the superscript $\pm$ designates the valley wherein the exciton is formed, μ is the reduced mass of the electron and hole, $E_{\sigma^\pm}$ are the circularly polarized components of the incident field, and $\psi'_{m\mathrm{p}}(0)$ denotes the derivative of the radial function of the mp-state with respect to the coordinate ρ of relative motion [cf. formula (40)]. In deriving formula (53), it is assumed that the light frequency is $\omega \approx E_{\mathrm{g}}/2\hbar$, and the binding energy of the exciton is disregarded in comparison with $\hbar\omega$.

Upon two-photon absorption, p-excitons that are transformed according to the representation Γ_6 are generated (see Section 3.4): in the case of σ^+-polarized light, a $2\mathrm{p}_+$-exciton in the $\mathbf{K}_+$ valley, and in the case of the σ^--polarized light, a $2\mathrm{p}_-$-exciton in the $\mathbf{K}_-$ valley. A schematic representation of this process is given in Fig. 15a: upon absorption of the first photon, an excitation of the ls-exciton occurs due to the

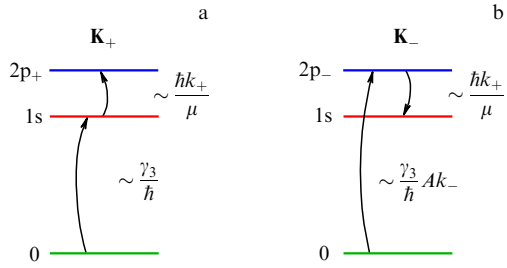

Figure 15. (Color online.) Illustration of two-photon absorption in MX_2 monolayers. Upon absorption of two σ^+-polarized photons, a $2\mathrm{p}_+$-exciton is generated in the $\mathbf{K}_+$ valley (a), and an 1s-exciton in the $\mathbf{K}_-$ valley (b). The corresponding matrix elements of the velocity operator are indicated near the transitions.

interband matrix element γ_3 of the velocity operator; the second photon causes transitions between 1s- and 2p-states of the exciton due to the velocity operator $\hbar k_\pm/\mu$ inside the band.

Measurements of photoluminescence under the conditions of the two-photon absorption [40, 65, 144] make it possible to experimentally estimate the energy gap between the 1s- and 2p-excitons in MX_2 monolayers, and also to investigate the details of the generation of the valley coherence of excitons and of the exciton–phonon interaction.

A special feature of the monolayers of dichalcogenides of transition metals is that these systems are noncentrosymmetrical and allow, as was discussed in Section 3.4, mixing of exciton states of different parities. Therefore, s-excitons can participate in two-photon absorption as well. The quadratic combination $E_{\omega,i} E_{\omega,j}$ of the fields that lie in the plane of the monolayer is transformed according to the reducible representation $\Gamma_6 \times \Gamma_6 = \Gamma_1 + \Gamma_2 + \Gamma_6$, which contains Γ_6 — the representation according to which the components of $E_{\omega,i}$ are transformed. Hence, s-excitons can participate in two-photon absorption as well; in this case, the absorption of two σ^+ (σ^-) photons is equivalent to the absorption of one σ^- (σ^+) photon.

Microscopically, the s-excitons can be excited due to the two-photon transitions that occur through the remote $\mathrm{c}+2$ and $\mathrm{v}-3$ bands. The corresponding contribution to the matrix element of an ns-exciton excitation is written down as

$$M^{(2,\pm)}_{n\mathrm{s}} = \left(\frac{e}{\omega}\right)^2 \frac{\gamma_3}{\hbar^2} A \psi^*_{n\mathrm{s}}(0) E^2_{\sigma^\mp}\,, \tag{54}$$

where the parameter A defined in formula (7) is responsible for the absence of the center of inversion. In the language of excitons, this two-stage process corresponds to the generation of a 2p-exciton due to the linear-in-$\mathbf{k}$ terms $\sim \gamma_3 A k_\pm/\hbar$ in the matrix element of the velocity operator [see formula (6)] and to its further transition into the 1s-state (see Fig. 15b). This process can be described as a two-stage transition with intermediate states in the remote $\mathrm{c}+2$ and $\mathrm{v}-3$ bands. The analysis performed in Ref. [69] shows that there is one additional contribution to the matrix element of s-exciton two-photon absorption, which is connected with the mixing of s- and p-excitons in the different valleys (see Section 3.4). The mixing of 1s- and mp-excitons, described by the parameters β_{1m} [cf. formula (37)], leads to a contribution $\sim \beta_{1m}/(E_{1\mathrm{s}} - E_{m\mathrm{p}}) M^{(2,\pm)}_{m\mathrm{p}}$ to the matrix element from the two-photon excitation of an ls-exciton.

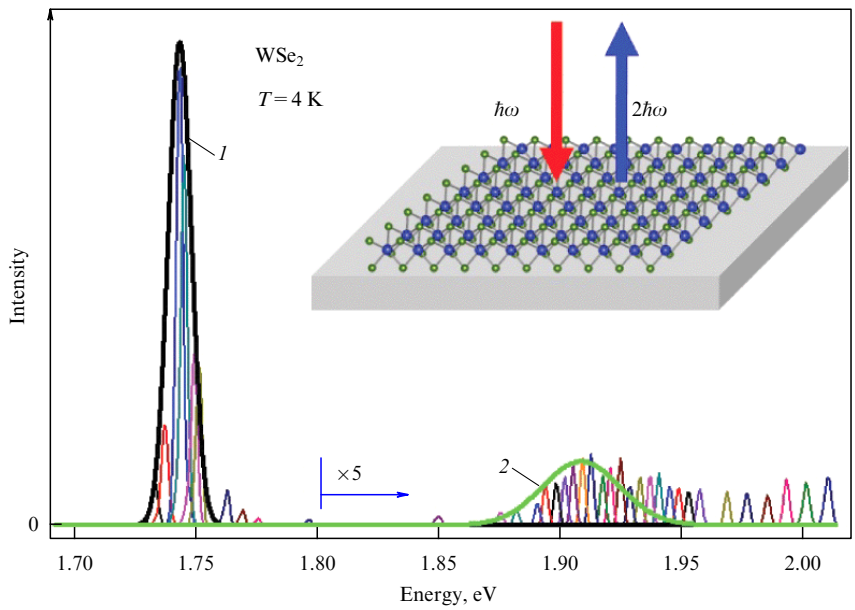

Figure 16. (Color online.) Spectrum of the generation of the second harmonic depending on the double energy of the quantum of radiation incident on the sample. The narrow peaks illustrate the spectrum measured at different (discrete) frequencies of excitation. The solid black (*1*) and green (*2*) curves show the results of fitting by Gaussian functions corresponding to the profiles of the transitions on 1s–2s/2p excitons. The intensity at energies greater than 1.8 eV is multiplied by 5. The inset demonstrates a schematic of the experiment. (Adapted from Ref. [69].)

One more experimentally investigated configuration of two-photon absorption in TMD monolayers is realized when $\hbar\omega$ is close to the excitation energy of the exciton. In that case, an intermediate state in the two-photon process proves to be real, and the efficiency of two-photon absorption strongly enhances in comparison with the nonresonance process. This effect can be responsible for summing up the radiation quanta (upconversion) in the WSe_2 monolayers observed in experiments [145].

In concluding this section, note that, as in many other semiconductors, a linear-circular dichroism of multiphoton absorption is expected in MX_2 monolayers [146–148]. For example, in ignoring the transitions through the remote v − 3 and c + 2 bands, the three-photon absorption coefficient is finite in the case of linear polarization, and it becomes zero in the case of circular polarization.

5.2 Generation of a second harmonic

The simultaneous optical activity of excitons in TMD monolayers in one- and two-photon processes leads to the efficient generation of a second optical harmonic [69, 149–151]. Phenomenologically, this effect at the normal incidence of light onto a monolayer of point symmetry D_{3h} is described by the following relationship [40, 69, 141, 152, 153]:

$$P_x^{(2\omega)} = 2\chi^{(2)} E_x E_y\,, \qquad P_y^{(2\omega)} = \chi^{(2)}(E_x^2 - E_y^2)\,, \tag{55}$$

where $\chi^{(2)}$ is the only nonzero component of the second-order nonlinear susceptibility. Microscopically, the generation of the second harmonic arises as a result of the excitation of an exciton in a two-photon process and its subsequent recombination with the emission of a photon. The microscopic theory developed in paper [69] shows that the basic contribution to the generation of the second harmonic comes from the 1s-exciton state. For the mechanism of this effect connected with the two-photon excitation of a 1s-exciton, shown in Fig. 15b, the expression for the resonance contribution to $\chi^{(2)}$ can be written out as [69]

$$\chi_{1s}^{(2)} = -\frac{e^3\left|\psi_{1s}(0)\right|^2}{\omega^2\omega_{1s}}\,A\left(\frac{\gamma_3}{\hbar}\right)^2\frac{1}{2\omega-\omega_{1s}+\mathrm{i}\Gamma_{1s}}\,, \tag{56}$$

where Γ_{1s} is the decay rate of the exciton, ω_{1s} is the frequency of the excitation of a 1s-exciton, and the parameter A is introduced in formula (7). Thus, the second-order susceptibility has a resonance at $\omega = \omega_{1s}/2$, when the real part of the denominator in formula (56) becomes zero. It is interesting that within the framework of the same mechanism the second-order nonlinear response of p-excitons has a smallness of $\sim E_{np}/E_g$, where E_{np} is the binding energy of the p-exciton with the principal quantum number n.

Experimentally, the generation of the second optical harmonic on the excitons in the monolayers of dichalcogenides of transition metals has been investigated in a number of studies [40, 154, 155]. Figure 16 presents experimental data on the excitation spectrum of the second harmonic taken from Refs [40, 69], where the enhancement of the generation of the second harmonic at the exciton resonances in a WSe_2 monolayer was studied. In this sample, the 2s- and 2p-exciton states were indistinguishable in the spectrum of the signal of the second harmonic, in spite of the fact that the calculations within the framework of the model of screened Coulomb interaction (Section 3) predicts their splitting equal to ~ 10 meV. An analysis of the experimental data shows that the main contribution to the generation of the second harmonic comes from the 1s-exciton state; its contribution integrally exceeds the contribution from the 2s/2p states by approximately an order of magnitude. This is in agreement with the model predictions of the microscopic theory presented above and in Ref. [69]. Detailed experimental and theoretical studies of the generation of the second harmonic and other nonlinear optical effects in TMD monolayers are among the most important problems for

future studies into the electronic and optical properties of such systems.

6. Conclusion

The physics of two-dimensional semiconductor crystals, in particular, of transition-metal dichalcogenides, is actively being developed. In this review, a description is given of the basic exciton properties common to the MoS_2, $MoSe_2$, WS_2, and WSe_2 monolayers, including large — on the order of several hundred millielectron-volts — binding energies of excitons, the deviation of an exciton series from the hydrogen-like one, and the unusual fine structures of exciton and trion energy levels connected with the presence of two valleys in the energy spectrum and spin-orbit splitting of bands. In these two-dimensional semiconductors, the excitons and trions play the key role in the formation of optical spectra and vividly manifest themselves in nonlinear optical effects. Many of the phenomena described in the review have already been discovered experimentally.

As further promising avenues of study, it is possible to choose a more detailed study of the fine structure and the effects of mixing the exciton states, the study of exciton transport [156], and the physics of exciton polaritons in van der Waals structures with microcavities [157–159]. There are a number of pioneering results in these areas; however, no detailed studies exist thus far. Furthermore, in our opinion, questions on the details of differences in the exciton effects showing themselves in similar at first glance two-dimensional semiconductors on the basis of molybdenum and tungsten are interesting and are still open.

Acknowledgments

The authors are deeply grateful to T Amand, G Wang, L E Golub, E L Ivchenko, X Marie, M Semina, A Chernikov, and B Urbazhek for the fruitful discussions. This study was supported in part by the Russian Science Foundation, project No. RNF 14-12-01067.

References

1. Novoselov K S et al. *Science* **306** 666 (2004)
2. Novoselov K S et al. *Nature* **438** 197 (2005)
3. Geim A K, Novoselov K S *Nature Mater*. **6** 183 (2007)
4. Lozovik Yu E, Merkulova S P, Sokolik A A *Phys. Usp*. **51** 727 (2008); *Usp. Fiz. Nauk* **178** 757 (2008)
5. Morozov S V, Novoselov K S, Geim A K *Phys. Usp*. **51** 744 (2008); *Usp. Fiz. Nauk* **178** 776 (2008)
6. Falkovsky L A *Phys. Usp*. **51** 887 (2008); *Usp. Fiz. Nauk* **178** 923 (2008)
7. Novoselov K S et al. *Proc. Natl. Acad. Sci. USA* **102** 10451 (2005)
8. Li L et al. *Nature Nanotechnol*. **9** 372 (2014)
9. Geim A K, Grigorieva I V *Nature* **499** 419 (2013)
10. Frindt R F *J. Appl. Phys*. **37** 1928 (1966)
11. Wilson J A, Yoffe A D *Adv. Phys*. **18** 193 (1969)
12. Yoffe A D, in *Festkörperprobleme 13* (Advances in Solid State Physics, Vol. 13, Ed. H J Queisser) (Berlin: Springer, 1973) p. 1
13. Mak K F et al. *Phys. Rev. Lett*. **105** 136805 (2010)
14. Splendiani A et al. *Nano Lett*. **10** 1271 (2010)
15. Kolobov A, Tominaga J *Two-Dimensional Transition-Metal Dichalcogenides* (Berlin: Springer, 2016)
16. Chernozatonskii L A, Artyukh A A *Phys. Usp*. **61** 2 (2018); *Usp. Fiz. Nauk* **188** 3 (2018)
17. Courtade E et al. *Phys. Rev. B* **96** 085302 (2017)
18. Kormányos A et al. *Phys. Rev. B* **88** 045416 (2013)
19. Kośmider K, González J W, Fernández-Rossier J *Phys. Rev. B* **88** 245436 (2013)
20. Liu G-B et al. *Phys. Rev. B* **88** 085433 (2013)
21. Mak K F et al. *Science* **344** 1489 (2014)
22. Mak K F et al. *Nature Nanotechnol*. **7** 494 (2012)
23. Cao T et al. *Nature Commun*. **3** 887 (2012)
24. Sallen G et al. *Phys. Rev. B* **86** 081301(R) (2012)
25. Zeng H et al. *Nature Nanotechnol*. **7** 490 (2012)
26. Xiao D et al. *Phys. Rev. Lett*. **108** 196802 (2012)
27. Chernikov A et al. *Phys. Rev. Lett*. **113** 076802 (2014)
28. He K et al. *Phys. Rev. Lett*. **113** 026803 (2014)
29. Ugeda M M et al. *Nature Mater*. **13** 1091 (2014)
30. Berkelbach T C, Hybertsen M S, Reichman D R *Phys. Rev. B* **88** 045318 (2013)
31. Mak K F et al. *Nature Mater*. **12** 207 (2013)
32. Courtade E et al. *Phys. Rev. B* **96** 085302 (2017)
33. Shi H et al. *Phys. Rev. B* **87** 155304 (2013)
34. Koster G F et al. *Properties of the Thirty-Two Point Groups* (Cambridge, Mass.: M.I.T. Press, 1963)
35. Wang G et al. *Nature Commun*. **6** 10110 (2015)
36. Komsa H-P, Krasheninnikov A V *Phys. Rev. B* **86** 241201(R) (2012)
37. Qiu D Y, da Jornada F H, Louie S G *Phys. Rev. Lett*. **111** 216805 (2013)
38. Molina-Sánchez A et al. *Phys. Rev. B* **88** 045412 (2013)
39. Fang S et al. *Phys. Rev. B* **92** 205108 (2015)
40. Wang G et al. *Phys. Rev. Lett*. **114** 097403 (2015)
41. Molina-Sánchez A, Hummer K, Wirtz L *Surf. Sci. Rep*. **70** 554 (2015)
42. Cappelluti E et al. *Phys. Rev. B* **88** 075409 (2013)
43. Ridolfi E et al. *J. Phys. Condens. Matter* **27** 365501 (2015)
44. Rostami H et al. *Phys. Rev. B* **92** 195402 (2015)
45. Rybkovskiy D V, Gerber I C, Durnev M V *Phys. Rev. B* **95** 155406 (2017)
46. Vurgaftman I, Meyer J R, Ram-Mohan L R *J. Appl. Phys*. **89** 5815 (2001)
47. Wang G et al. *2D Mater*. **2** 034002 (2015)
48. Frenkel J *Phys. Rev*. **37** 17 (1931)
49. Frenkel J *Phys. Rev*. **37** 1276 (1931)
50. Wannier G H *Phys. Rev*. **52** 191 (1937)
51. Mott N F *Proc. R. Soc. Lond. A* **167** 384 (1938)
52. Gross E F, Karryev N A *Dokl. Akad. Nauk SSSR* **84** 261 (1952)
53. Rytova N S *Moscow Univ. Phys. Bull*. **22** (3) 18 (1967); *Vestn. Mosk. Gos. Univ. Ser. Fiz*. (3) 30 (1967)
54. Keldysh L V *JETP Lett*. **29** 658 (1979); *Pis'ma Zh. Eksp. Teor. Fiz*. **29** 716 (1979)
55. Landau L D, Lifshitz E M *Electrodynamics of Continuous Media* (Oxford: Butterworth-Heinemann, 2004); Translated from Russian: *Elektrodinamika Sploshnykh Sred* (Moscow: Nauka, 1992)
56. Agranovich V M, Ginzburg V G *Crystal Optics with Spatial Dispersion, and Excitons* (Berlin: Springer-Verlag, 1984); Translated from Russian: *Kristallooptika s Uchetom Prostranstvennoi Dispersii i Teoriya Eksitonov* (Moscow: Nauka, 1965)
57. Cudazzo P, Tokatly I V, Rubio A *Phys. Rev. B* **84** 085406 (2011)
58. Rashba E I, Sturge M D (Eds) *Excitons* (Modern Problems in Condensed Matter Sciences, Vol. 2) (Amsterdam: North-Holland, 1982)
59. Glutsch S G *Excitons in Low-Dimensional Semiconductors* (Berlin: Springer-Verlag, 2004)
60. Ivchenko E L, Pikus G E *Superlattices and other Heterostructures* (Berlin: Springer, 1997)
61. Ivchenko E L *Optical Spectroscopy of Semiconductor Nanostructures* (Harrow, UK: Alpha Science, 2005)
62. Bir G L, Pikus G E *Symmetry and Strain-Induced Effects in Semiconductors* (New York: Wiley, 1974)
63. Glazov M M et al. *Phys. Status Solidi B* **252** 2349 (2015)
64. Bir G L, Pikus G E *Simmetriya i Deformatsionnye Effekty v Poluprovodnikakh* (Symmetry and Strain-Induced Effects in Semiconductors) (Moscow: Nauka, 1972)
65. Ye Z et al. *Nature* **513** 214 (2014)
66. Stier A V et al. *Nano Lett*. **16** 7054 (2016)
67. Lin Y et al. *Nano Lett*. **14** 5569 (2014)
68. Wu F, Qu F, MacDonald A H *Phys. Rev. B* **91** 075310 (2015)
69. Glazov M M et al. *Phys. Rev. B* **95** 035311 (2017)
70. Wang G et al. *Phys. Rev. Lett*. **119** 047401 (2017)
71. Denisov M M, Makarov V P *Phys. Status Solidi B* **56** 9 (1973)
72. Echeverry J P et al. *Phys. Rev. B* **93** 121107(R) (2016)

73. Qiu D Y, Cao T, Louie S G *Phys. Rev. Lett.* **115** 176801 (2015)
74. Dery H, Song Y *Phys. Rev. B* **92** 125431 (2015)
75. Zhang X-X et al. *Phys. Rev. Lett.* **115** 257403 (2015)
76. Arora A et al. *Nanoscale* **7** 10421 (2015)
77. Withers F et al. *Nano Lett.* **15** 8223 (2015)
78. Slobodeniuk A O, Basko D M *2D Mater.* **3** 035009 (2016)
79. Glazov M M et al. *Phys. Rev. B* **89** 201302(R) (2014)
80. Yu H et al. *Nature Commun.* **5** 3876 (2014)
81. Yu T, Wu M W *Phys. Rev. B* **89** 205303 (2014)
82. Maialle M, de Andrada e Silva E, Sham L J *Phys. Rev. B* **47** 15776 (1993)
83. Ivchenko E L *Phys. Status Solidi A* **164** 487 (1997)
84. Goupalov S V, Ivchenko E L, Kavokin A V *JETP* **86** 388 (1998); *Zh. Eksp. Teor. Fiz.* **113** 703 (1998)
85. Dyakonov M I (Ed.) *Spin Physics in Semiconductors* (Berlin: Springer-Verlag, 2008)
86. Berkelbach T C, Hybertsen M S, Reichman D R *Phys. Rev. B* **92** 085413 (2015)
87. Srivastava A, Imamoğlu A *Phys. Rev. Lett.* **115** 166802 (2015)
88. Zhou J et al. *Phys. Rev. Lett.* **115** 166803 (2015)
89. Berghäuser G, Knorr A, Malic E *2D Mater.* **4** 015029 (2017)
90. Lampert M A *Phys. Rev. Lett.* **1** 450 (1958)
91. Stébé B, Ainane A *Superlatt. Microstruct.* **5** 545 (1989)
92. Kheng K et al. *Phys. Rev. Lett.* **71** 1752 (1993)
93. Finkelstein G, Shtrikman H, Bar-Joseph I *Phys. Rev. B* **53** R1709 (1996)
94. Thilagam A *Phys. Rev. B* **55** 7804 (1997)
95. Sergeev R A, Suris R A *Phys. Solid State* **43** 746 (2001); *Fiz. Tverd. Tela* **43** 714 (2001)
96. Ross J S et al. *Nature Commun.* **4** 1474 (2013)
97. Landau L D, Lifshitz E M *Quantum Mechanics: Non-Relativistic Theory* (Oxford: Pergamon Press, 1977); Translated from Russian: *Kvantovaya Mekhanika. Nerelyativistskaya Teoriya* (Moscow: Nauka, 1989)
98. Ganchev B et al. *Phys. Rev. Lett.* **114** 107401 (2015)
99. Szyniszewski M et al. *Phys. Rev. B* **95** 081301(R) (2017)
100. Sergeev R A, Suris R A *Phys. Status Solidi B* **227** 387 (2001)
101. Jones A M et al. *Nature Phys.* **12** 323 (2016)
102. Plechinger G et al. *Nature Commun.* **7** 12715 (2016)
103. Danovich M, Zólyomi V, Fal'ko V I *Sci. Rep.* **7** 45998 (2017)
104. Suris R A et al. *Phys. Status Solidi B* **227** 343 (2001)
105. Suris R A, in *Optical Properties of 2D Systems with Interacting Electrons* (NATO Science Series, Ser. II, Vol. 119, Eds W J Ossau, R A Suris) (Dordrecht: Kluwer Acad. Publ., 2003) p. 111
106. Efimkin D K, MacDonald A H *Phys. Rev. B* **95** 035417 (2017)
107. Sidler M et al. *Nature Phys.* **13** 255 (2017)
108. Li Y et al. *Phys. Rev. Lett.* **113** 266804 (2014)
109. Srivastava A et al. *Nature Phys.* **11** 141 (2015)
110. Aivazian G et al. *Nature Phys.* **11** 148 (2015)
111. Stier A V et al. *Nature Commun.* **7** 10643 (2016)
112. Cadiz F et al. *Phys. Rev. X* **7** 021026 (2017)
113. Jones A M et al. *Nature Nanotechnol.* **8** 634 (2013)
114. Lagarde D et al. *Phys. Rev. Lett.* **112** 047401 (2014)
115. Zhu C R et al. *Phys. Rev. B* **90** 161302(R) (2014)
116. Wang G et al. *Phys. Rev. Lett.* **117** 187401 (2016)
117. Tokman M, Wang Y, Belyanin A *Phys. Rev. B* **92** 075409 (2015)
118. Meier F, Zakharchenya B (Eds) *Optical Orientation* (Amsterdam: Horth-Holland, 1984); Translated into Russian: Zakharchenya B P, Meier F (Eds) *Opticheskaya Orientatsiya* (Leningrad: Nauka, 1989)
119. Maialle M Z *Phys. Rev. B* **61** 10877 (2000)
120. Lhuillier C, Laloë F *J. Phys. France* **43** 197 (1982)
121. Lhuillier C, Laloë F *J. Phys. France* **43** 225 (1982)
122. Glazov M M et al. *Solid State Commun.* **134** 117 (2005)
123. Krizhanovskii D N et al. *Phys. Rev. B* **73** 073303 (2006)
124. Glazov M M *Phys. Solid State* **54** 1 (2012); *Fiz. Tverd. Tela* **54** 3 (2012)
125. Dyakonov M I, Perel' V I *Sov. Phys. Solid State* **13** 3023 (1972); *Fiz. Tverd. Tela* **13** 3581 (1971)
126. Poellmann C et al. *Nature Mater.* **14** 889 (2015)
127. Robert C et al. *Phys. Rev. B* **93** 205423 (2016)
128. Sun D et al. *Nano Lett.* **14** 5625 (2014)
129. Mouri S et al. *Phys. Rev. B* **90** 155449 (2014)
130. Yu Y et al. *Phys. Rev. B* **93** 201111(R) (2016)
131. Hoshi Y et al. *Phys. Rev. B* **95** 241403(R) (2017)
132. Moody G et al. *Nature Commun.* **6** 8315 (2015)
133. Selig M et al. *Nature Commun.* **7** 13279 (2016)
134. Plechinger G et al., arXiv:1404.7674
135. McCormick E J et al. *2D Mater.* **5** 011010 (2016)
136. Dey P et al. *Phys. Rev. Lett.* **119** 137401 (2017)
137. Singh A et al. *Phys. Rev. Lett.* **117** 257402 (2016)
138. Belinicher V I, Sturman B I *Sov. Phys. Usp.* **23** 199 (1980); *Usp. Fiz. Nauk* **130** 415 (1980)
139. Bloembergen N *Nonlinear Optics* 4th ed. (Singapore: World Scientific, 1996)
140. Ganichev S D, Prettl W *Intense Terahertz Excitation of Semiconductors* (Oxford: Oxford Univ. Press, 2006)
141. Glazov M M, Ganichev S D *Phys. Rep.* **535** 101 (2014)
142. Rashba E I, Sturge M D (Eds) *Excitons* (Amsterdam: North-Holland, 1982); Translated into Russian: *Eksitony* (Excitons) (Moscow: Nauka, 1985)
143. Mahan G D *Phys. Rev.* **170** 825 (1968)
144. Wang G et al. *Phys. Rev. Lett.* **115** 117401 (2015)
145. Manca M et al. *Nature Commun.* **8** 14927 (2017)
146. Ivchenko E L, Perlin E Yu *Sov. Phys. Solid State* **15** 1850 (1974); *Fiz. Tverd. Tela* **15** 2781 (1973)
147. Arifzhanov S B, Ivchenko E L *Sov. Phys. Solid State* **17** 46 (1975); *Fiz. Tverd. Tela* **17** 81 (1975)
148. Danishevskii A M, Kochegarov S F, Subashiev V K *JETP* **43** 83 (1976); *Zh. Eksp. Teor. Fiz.* **70** 158 (1976)
149. Pedersen T G, Cornean H D *Europhys. Lett.* **78** 27005 (2007)
150. Trolle M L, Seifert G, Pedersen T G *Phys. Rev. B* **89** 235410 (2014)
151. Grüning M, Attaccalite C *Phys. Rev. B* **89** 081102(R) (2014)
152. Golub L E et al. *Phys. Rev. B* **84** 195408 (2011)
153. Golub L E, Tarasenko S A *Phys. Rev. B* **90** 201402(R) (2014)
154. Trolle M L et al. *Phys. Rev. B* **92** 161409(R) (2015)
155. Seyler K L et al. *Nature Nanotechnol.* **10** 407 (2015)
156. Rivera P et al. *Science* **351** 688 (2016)
157. Liu X et al. *Nature Photon.* **9** 30 (2015)
158. Dufferwiel S et al. *Nature Commun.* **6** 8579 (2015)
159. Lundt N et al. *Nature Commun.* **7** 13328 (2016)